

Neutron Stars and Gravitational Waves: the Key Role of Nuclear Equation of State

Polychronis S. Koliogiannis ^{1,†,‡,*} , Alkiviadis Kanakis-Pegios ^{1,†,‡}  and Charalampos C. Moustakidis ^{1,†,‡} 

¹ Department of Theoretical Physics, Aristotle University of Thessaloniki, 54124 Thessaloniki, Greece; alkanaki@auth.gr (A.K.P.); moustaki@auth.gr (C.C.M.)

* Correspondence: pkoliogi@physics.auth.gr

† Current address: Aristotle University of Thessaloniki, 54124, Greece

‡ These authors contributed equally to this work.

Abstract: Neutron stars are the densest known objects in the universe and an ideal laboratory for the strange physics of super-condensed matter. Theoretical studies in connection with recent observational data of isolated neutron stars, as well as binary neutron stars systems, offer an excellent opportunity to provide robust solutions on the dense nuclear problem. In the present work, we review our recently studies concerning the applications of various theoretical nuclear models on a few recent observations of binary neutron stars or neutron star black hole systems. In particular, using a simple and well established model, we parametrize the stiffness of the equation of state with the help of the speed of sound. Moreover, in comparison to the recent observations of two events by LIGO/VIRGO collaboration, GW170817 and GW190425, we suggest possible robust constraints. We also concentrate our theoretical study on the recent observation of a compact object with mass $\sim 2.59^{+0.08}_{-0.09} M_{\odot}$ (GW190814 event), as a component of a system where the main companion was a black hole with mass $\sim 23 M_{\odot}$. A scientific debate initiated concerning the identification of the low mass component, as it falls into the neutron star - black hole mass gap. This is an important issue since the understanding of the nature of GW190814 event will offer rich information concerning the upper limit of the speed of sound in dense matter and the possible phase transition into other degrees of freedom. We systematically study the tidal deformability of a possible high mass candidate existing as an individual star or as a component one in a binary neutron star system. Finally, we provide some applications of equations of state of hot, dense nuclear matter in hot neutron stars (nonrotating and rapidly rotating with the Kepler frequency neutron stars), protoneutron stars, and binary neutron star merger remnants.

Keywords: neutron stars; nuclear equation of state; gravitational waves; speed of sound; tidal polarizability.

PACS: 26.60.-c, 21.30.Fe, 21.65.Cd, 26.60.Kp



Citation: Koliogiannis, P.; Kanakis-Pegios, A.; Moustakidis, C. Neutron stars and gravitational waves: the key role of nuclear equation of state. *Preprints* **2021**, *1*, 0. <https://doi.org/>

Received:

Accepted:

Published:

Publisher's Note: MDPI stays neutral with regard to jurisdictional claims in published maps and institutional affiliations.

1. Introduction

One of the unsolved open problems currently in Nuclear Physics is the study of dense nuclear matter properties. Especially, compact objects such as white dwarfs and mainly neutron stars offer the opportunity to study the behavior of nuclear matter in high densities [1–4]. Neutron stars are a very promising tool for studying the properties of dense nuclear matter, such as the speed of sound and its possible upper bound.

The main assumption for the speed of sound is that cannot exceed the speed of light because of the causality. Although, this is not determinant as Zel'dovich [5,6] showed the importance to define a rigorous speed of sound limit upon the equation of state (EoS). To be more specific, in the electromagnetic interaction the main assumption is that $v_s \leq c/\sqrt{3}$ is a general law of nature. Moreover, by considering the interaction of baryons through a vector field, he noticed that the upper limit of the speed of sound is the causality, $v_s = c$. Therefore,

the only restriction imposed by general principles is that $v_s \leq c$ [5,6]. On the other hand, Hartle noticed that the causality is not enough to constrain the high-density part of the EoS [7], while Weinberg pointed out that the speed of sound is much less than the speed of light for a cold nonrelativistic fluid [4]. In addition, for nonrelativistic and/or weakly coupled theories the bound $v_s = c/\sqrt{3}$ according to Bedaque and Steiner seems to be valid, while in conformal theories the upper bound is saturated [8]. According to the authors, the existence of two solar masses neutron stars, in combination with the knowledge of the EoS of hadronic matter at the low density region, is not consistent with the limit $c/\sqrt{3}$. We notice that recently various studies have been made regarding the speed of sound and the tidal deformability of neutron stars [9–12].

One of the goals of this study is to apply a method that directly relates the observed tidal deformability, derived from binary neutron stars mergers, to the maximum mass of neutron stars aiming to obtain constraints on the upper bound of the speed of sound. The main idea is the fact that while the measured upper limit of the effective tidal deformability favors softer EoSs, the recent measurements of high neutron star masses favor stiffer EoSs. As a basis in our study, we used a model in which we parametrized the EoS through the various bounds of the speed of sound (stiffness). Hence, the EoS is a functional of the transition density and the speed of sound bound. In our approach, we used the observation of the two recent events, GW170817 [13] and GW190425 [14], as well as the current observed maximum neutron star masses ($1.908 \pm 0.016 M_\odot$ [15], $2.01 \pm 0.04 M_\odot$ [16], $2.14^{+0.10}_{-0.09} M_\odot$ [17] and $2.27^{+0.17}_{-0.15} M_\odot$ [18]). The need for (a) a soft EoS for the low density region (to be in accordance with the observed upper limit of the effective tidal deformability) and (b) a stiff EoS for the high density region (to provide the high neutron star masses) leads to robust constraints on the EoS. In addition, this method allows making postulations about the kind of future measurements that would be more informative and help to improve our knowledge.

Furthermore, we remark the very recent observation of the GW190814 event, where a gravitational wave has been detected from the merger of a $22.2 - 24.3 M_\odot$ black hole with a non-identified compact object with mass $2.5 - 2.67 M_\odot$ [19,20]. Although the authors of the mentioned references suggest that is unlikely the secondary mass to belong to a neutron star, they do leave *open the window* that the improved knowledge of the neutron star EoS and further observations of the astrophysical population of compact objects could alter this assessment.

It is worth to point out that the observation of the GW190814 event has some additional general benefits apart from the measurement of $2.6 M_\odot$ of the second partner [19]. Firstly, this binary system has the most unequal mass ratio yet measured with gravitational waves close to the value of 0.112. Secondly, the dimensionless of the spin of the primary black hole is constrained to ≤ 0.07 , where various tests of general relativity confirm this value, as well as its predictions of higher multiple emissions at high confidence interval. Moreover, the GW190814 event poses a challenge for the understanding of the population of merging compact binaries. It was found, after systematic analysis, that the merger rate density of GW190814-like binary system to be $7^{+16}_{-6} \text{ Gpc}^{-3} \text{ yr}^{-1}$ [19]. More relevant to the present study, the observation of the GW190814 event led to the following conclusion: due to the source's asymmetric masses, the lack of detection of an electromagnetic counterpart and of clear signature of tides or spin-induced quadrupole effect in the waveform of the gravitational waves, we are not able to distinguish between a black hole-black hole and black hole-neutron star system [19]. In this case, one must count only to the comparison between the mass of the second partner with the estimation of maximum neutron star mass [21]. This is one of the main subjects which revised in the present work. It should be emphasized that the measurements of neutron star mass can also inform us about a bound on the maximum gravitational mass independently of the assumptions of specific EoS. For example, Alsing *et al.* [22] fitting the known population

of neutron stars in binaries to double-Gaussian mass distribution, obtained the empirical constraint that $M_{\max} \leq 2.6 M_{\odot}$ (with 90% confidence interval).

Farr and Chatziionannou updated previous studies including recent measurements [23]. Their study constraint the maximum mass $M_{\max} = 2.25^{+0.81}_{-0.26} M_{\odot}$ leading to the conclusion that the posterior probability (for the mass of the second partner $m_2 \leq M_{\max}$) is around only 29%. However, the prediction of M_{\max} is sensitive on the selection rules mass of neutron star (not only on binary systems but also isolated) as well as on the discovery of new events and consequently, remains an open problem. Finally, the conclusion of the recent GW190814 event in comparison with previous ones (for example the GW170817 event [24]) may shed light on the problem of the M_{\max} . For example, the spectral EoSs which are conditioned by the GW170817 event, are once more elaborated to include the possibility that of the prediction of M_{\max} at least equal to m_2 . This approach lead to significant constraints on the radius and tidal deformability of a neutron star with mass of $1.4 M_{\odot}$ ($R_{1.4} = 12.9^{+0.8}_{-0.7}$ km and $\Lambda_{1.4} = 616^{+273}_{-158}$ respectively [19]).

The matter of the finite temperature and its effect on the nuclear EoS, as well as astrophysical applications, has been extensively studied by Bethe *et al.* [25], Brown *et al.* [26], Lamb *et al.* [27], Lattimer and Ravenhall [28] and Lattimer [29]. Lattimer and Swesty [30], as well as Shen *et al.* [31], have constructed the most used hot neutron star EoSs. The first one is based on the liquid drop-type model and the second one is based on the relativistic mean field model. Afterwards, Shen *et al.* [31] broadened their study in order to study supernovae, binary neutron star mergers, and black hole formations by developing EoSs for various temperatures and proton fractions [32]. In addition, the density and temperature dependence of the nuclear symmetry free energy using microscopic two- and three-body nuclear potentials constructed from Chiral effective field theory have been studied in a series of work, including the one of Wellenhofer *et al.* [33]. Furthermore, hot neutron star and supernova properties have been studied by Constantinou *et al.* [34,35], where a suitable hot EoS is produced. Finally, the interplay between the temperature and the neutron star matter were probed by Sammarruca *et al.* [36], by considering the framework of Chiral effective field theory.

EoSs at finite temperature constructed within the Brueckner-Hartree-Fock approach and the properties of hot β -stable nuclear matter had been studied in a series of papers [37–45]. In addition, a model for cold nucleonic EoSs extended to include temperature and proton fractions, where simulations of astrophysical phenomena use, has been constructed by Raithel *et al.* [46]. Pons *et al.* [47], as well as Prakash *et al.* [48], focused on describing the thermal and chemical evolution of protoneutron stars, by considering neutrino opacities consistently calculated with the EoS. Finally, neutron stars along with the hot EoS of dense matter, are presented in a recent review of Lattimer and Prakash [49].

The processes that occupy the stages of the merger and postmerger phases of a binary neutron star system have been extensively studied in the last years. However, matters that concern the remnant evolution are still under consideration, or even unsolved. In particular, the remnant evolution contains (a) the collapse time, (b) the threshold mass, (c) the possible phase transition in the interior of the star, and (d) the disk ejecta and neutrino emission (for an extended discussion and applications, see Perego *et al.* [50]). It has to be noted here that the possibility of a phase transition will effect the signal of the emitted gravitational wave. Relevant previous work is also be available in Bauswein *et al.* [51], Kaplan *et al.* [52], Tsokaros *et al.* [53], Yasin *et al.* [54], Radice *et al.* [55], Sarin *et al.* [56], Soma and Bandyopadhyay [57], and Sen [58].

In the present work we review some applications of the thermal effects on neutron star properties. In particular, we apply a momentum-dependent effective interaction (MDI) model, where thermal effects can be studied simultaneously on the kinetic part of the energy and also on the interaction one. In addition, the extension of the proposed model can lead to EoSs with

varying stiffness with respect to the parameterized symmetry energy. In fact, Gale *et al.* [59] presented the model aimed at the influence of MDI on the momentum flow of heavy-ion collisions. However, the model has been successfully applied in studying the properties of cold and hot nuclear and neutron star matter (for an extensive review of the model, see Refs. [60–62]).

Moreover, we review specific properties of neutron stars (including mainly the mass and radius, moment of inertia, Kerr parameter, etc.), with respect to the EoS, both at nonrotating and rapidly rotating (considering the mass-shedding limit) configurations. The above properties are well applied in studying hot neutron stars, protoneutron stars, as well as the remnant of a binary neutron star system.

Summarizing, in the present work we review the applications of various theoretical nuclear models on a few recent observations of binary neutron stars or neutron star black hole systems including mainly the GW170817, GW190425 and GW190814 events. Our results have been published recently in sections, in the following journals [63–66].

It has to be noted that the present study is mainly dedicated to the case of the emission of the gravitation waves due to the merger of a binary neutron star system. However, there are other mechanisms by which gravitational waves are emitted by a neutron star and thus, have additional ways of studying its internal structure (for a recent review see Ref. [67]). These mechanisms, that considered as continuous gravitational waves sources, include for example (a) the case of radiation of gravitational waves by a rigidly rotating aligned triaxial ellipsoid (radiation of purely quadrupolar waves), (b) the emission of gravitational waves due to asymmetry in the magnetic field distribution in the interior of the neutron star, and (c) the radiation of gravitational waves from the rapidly rotating neutron stars. In this case, neutron stars may suffer a number of instabilities which come in different which they have a general feature in common that is they can be directly associated with unstable modes of oscillation (for exable g-modes, f-modes, w-modes, r-modes; for a review see Ref. [68]). The more notable mechanism is the r-mode oscillations. In these oscillations the restoring force is the Coriolis force. The r-mode mechanics has been proposed as an explanation for the observed relatively low spin frequencies of young neutron stars, as well as of accreting neutron stars in low-mass X-ray binaries. This instability only occurs when the gravitational radiation driving timescale is shorter compared to the ones of the various dissipation mechanisms which occur in the neutron star matter [69]. The free precession which may cause deformation of the neutron star leading to a better understanding of some neutron star matter properties, including breaking strain, viscosity, rigidity and elasticity [67]. We expect that in the future, the development of the sensitivity of LIGO and Virgo detectors in cooperation with and new instruments will help significantly to improve our knowledge of neutron star interior with the detection of the emitted gravitational waves [67].

Another way to study the properties of dense nuclear matter that exists inside neutron stars can be done with the help of the statistical study of the observed properties of neutron stars. To be more specific, we refer to the observational data concerning both isolated neutron stars and those that exist in binary systems. In the first case, there are extensive studies where observational data are applied to estimations with the help of statistical studies, for example the maximum possible mass of a neutron star, but mainly the radius of a neutron star with a mass of about $1.4 M_{\odot}$. In each case, valuable information and ideas can be extracted and utilized in terms of knowledge of the EoS of neutron star matter, in order to evaluate the reliability of the existing EoS (see the review article [70] and references therein). In the case of binary systems, the analysis of the emitted gravitational waves from the fusion of a binary system of neutron stars, where a large amount of information is received by studying the amplitude and phase of gravitational waves, is utilized. These studies mainly focus on the measurement (and utilization of the measurement) of tidal deformability. In any case, extensive

and systematic statistical estimation of data can lead to valuable knowledge of the structure and composition of neutron stars (for a recent review see [71] and references therein).

The article is organized as follows: in Section 2, we present the theory concerning the equation of state and the structure of the cold neutron stars. In Section 3, we present the construction of the hot equations of state (both isothermal and isoentropic) and briefly discuss the stability equation of hot rapidly rotating neutron star. The results and the discussion are provided in Section 4, while Section 5 includes the most noteworthy concluding remarks of the present review.

2. Cold Neutron Stars

2.1. The Momentum-Dependent Interaction Nuclear Model

The description of the interior structure of neutron stars demands the use of a nuclear model suitable to describe the properties of dense nuclear matter. In the present work, the EoS of nuclear matter is studied using a momentum dependent interaction (MDI) model. In this model, the energy per baryon is given by the formulae [72,73]

$$\begin{aligned}
 E(n, I) = & \frac{3}{10} E_F^0 u^{2/3} [(1+I)^{5/3} + (1-I)^{5/3}] + \frac{1}{3} A \left[\frac{3}{2} - X_0 I^2 \right] u + \frac{\frac{2}{3} B \left[\frac{3}{2} - X_3 I^2 \right] u^\sigma}{1 + \frac{2}{3} B' \left[\frac{3}{2} - X_3 I^2 \right] u^{\sigma-1}} \\
 & + \frac{3}{2} \sum_{i=1,2} \left[C_i + \frac{C_i - 8Z_i}{5} I \right] \left(\frac{\Lambda_i}{k_F^0} \right)^3 \left(\frac{((1+I)u)^{1/3}}{\frac{\Lambda_i}{k_F^0}} - \tan^{-1} \frac{((1+I)u)^{1/3}}{\frac{\Lambda_i}{k_F^0}} \right) \\
 & + \frac{3}{2} \sum_{i=1,2} \left[C_i - \frac{C_i - 8Z_i}{5} I \right] \left(\frac{\Lambda_i}{k_F^0} \right)^3 \left(\frac{((1-I)u)^{1/3}}{\frac{\Lambda_i}{k_F^0}} - \tan^{-1} \frac{((1-I)u)^{1/3}}{\frac{\Lambda_i}{k_F^0}} \right), \quad (1)
 \end{aligned}$$

where u is the baryon density normalized with respect to the saturation density $n_s = 0.16 \text{ fm}^{-3}$, $I = (n_n - n_p)/n$ is the asymmetry parameter, $X_0 = x_0 + 1/2$, and $X_3 = x_3 + 1/2$. The parameters A , B , σ , C_i , and B' appear in the description of symmetric nuclear matter (SNM) and are determined so that the relation $E(n_s, 0) = -16 \text{ MeV}$ holds. Λ_1 and Λ_2 are finite range parameters equal to $1.5k_F^0$ and $3k_F^0$, respectively, where k_F^0 being the Fermi momentum at the saturation density. The remaining parameters, x_0 , x_3 , Z_i , appear in the description of asymmetric nuclear matter and, with a suitable parametrization, are used in order to obtain different forms for the density dependence of symmetry energy, as well as the value of the slope parameter L and the value of the symmetry energy E_{sym} at the saturation density, defined as [63]

$$L = 3n_s \frac{dE_{\text{sym}}(n)}{dn} \Big|_{n_s} \quad \text{and} \quad E_{\text{sym}}(n) = \frac{1}{2} \frac{\partial^2 E(n, I)}{\partial I^2} \Big|_{I=0}, \quad (2)$$

and as a consequence different parametrizations of the EoS stiffness.

The specific choice of the MDI model is based on that (a) it combines both density and momentum dependent interaction among the nucleons, (b) it is suitable for studying neutron star matter at zero and finite temperature (due to the momentum term), (c) it reproduces with high accuracy the properties of SNM at the saturation density, including isovector quantities, (d) it reproduces the microscopic properties of the Chiral model for pure neutron matter (PNM) and the results of *state-of-the-art* calculations of Akmal *et al.* [74] with suitable parametrizations, (e) it predicts maximum neutron star mass higher than the observed ones [16–18], and (f) it maintains the causal behavior of the EoS even at densities higher than the ones that correspond to the maximum mass configuration.

2.2. Speed of Sound Formalism

An EoS can be parametrized in order to reproduce specific values of the speed of sound in the interior of the neutron star. This parametrization is possible following the formula available through Refs. [22,75–81]

$$P(\mathcal{E}) = \begin{cases} P_{\text{crust}}(\mathcal{E}), & \mathcal{E} \leq \mathcal{E}_{\text{c-edge}} \\ P_{\text{NM}}(\mathcal{E}), & \mathcal{E}_{\text{c-edge}} \leq \mathcal{E} \leq \mathcal{E}_{\text{tr}} \\ \left(\frac{v_s}{c}\right)^2(\mathcal{E} - \mathcal{E}_{\text{tr}}) + P_{\text{NM}}(\mathcal{E}_{\text{tr}}), & \mathcal{E}_{\text{tr}} \leq \mathcal{E}, \end{cases} \quad (3)$$

where P and \mathcal{E} denote the pressure and the energy density, respectively, and the corresponding subscript "tr" in energy density, denotes the energy density at the transition density.

However, following the approach in Eq. (3), only the continuity in the EoS is ensured. The artificial character of Eq. (3) does not take into account the continuity in the speed of sound. Therefore, in order to ensure the continuity and a smooth transition, we followed the method presented in Ref. [82]. We proceeded with the matching of the EoSs on the transition density by considering that, above this value, the speed of sound is parametrized as follows (for more details see Ref. [82])

$$\frac{v_s}{c} = \left(a - c_1 \exp \left[-\frac{(n - c_2)^2}{w^2} \right] \right)^{1/2}, \quad a \in [1/3, 1] \quad (4)$$

where the parameters c_1 and c_2 are fit to the speed of sound and its derivative at n_{tr} , and also to the demands $v_s(n_{\text{tr}}) = [c/\sqrt{3}, c]$ [75] according to the value of α . The remaining parameter w controls the width of the curve, where in our case is equal to 10^{-3} fm^{-3} in order to preserve the neutron star properties. Using Eq. (4), the EoS for $n \geq n_{\text{tr}}$ can be constructed with the help of the following recipe [82]

$$\mathcal{E}_{i+1} = \mathcal{E}_i + \Delta\mathcal{E}, \quad P_{i+1} = P_i + \left(\frac{v_s}{c}(n_i)\right)^2 \Delta\mathcal{E}, \quad (5)$$

$$\Delta\mathcal{E} = \Delta n \left(\frac{\mathcal{E}_i + P_i}{n_i} \right), \quad (6)$$

$$\Delta n = n_{i+1} - n_i. \quad (7)$$

2.3. Construction of the EoS

The construction of the EoS for the interior of neutron stars is based on the MDI model and data provided by Akmal *et al.* [74]. More specifically, we utilized the data for the A18+UIX (hereafter APR-1) EoS from Akmal *et al.* [74] for the energy per particle of SNM and PNM in the density range $[0.04, 0.96] \text{ fm}^{-3}$. Due to the complexity of the microscopic data, we divided the density region in three sections: (a) low-density region $[0.04, 0.2] \text{ fm}^{-3}$, (b) medium-density region $[0.2, 0.56] \text{ fm}^{-3}$, and (c) high-density region $[0.56, 0.96] \text{ fm}^{-3}$, in order to acquire the best fitting using Eq. (1). From this process emerged the coefficients for the SNM and ANM, and eventually the EoS, hereafter MDI-APR.

In the case of the speed of sound parametrized EoSs, the construction of the EoSs follows the procedure: (a) in region $\mathcal{E} \leq \mathcal{E}_{\text{c-edge}}$, we used the equation of Feynman *et al.* [83] and also of Baym *et al.* [84] for the crust and low densities of neutron star, (b) in the intermediate region, $\mathcal{E}_{\text{c-edge}} \leq \mathcal{E} \leq \mathcal{E}_{\text{tr}}$, we employed the MDI-APR EoS, and (c) for $\mathcal{E}_{\text{tr}} \leq \mathcal{E}$ region, the EoS is maximally stiff with the speed of sound, defined as $v_s = c\sqrt{(\partial P/\partial \mathcal{E})_S}$ (where S is the entropy) fixed in the present work in the range $[c/\sqrt{3}, c]$. The lowest allowed value of the speed of

sound, that is $(v_s/c)^2 = 1/3$, is introduced in order to be consistent with the possibility of a phase transition in quark matter. In this case, the theoretical predictions lead to this value as an upper bound of the speed of sound. The implementation of speed of sound values between the limited ones will lead to results well constrained by the two mentioned limits. Although the energy densities below the $\mathcal{E}_{c\text{-edge}}$ have negligible effects on the maximum mass configuration, we used them in calculations for the accurate estimation of the tidal deformability.

In this study, two cases, based on the transition density, $n_{\text{tr}} = pn_s$, and the speed of sound, are employed. In particular, (a) the ones where p takes the values $[1.5, 2, 3, 4, 5]$, while the speed of sound is parametrized in the two limiting cases, $(v_s/c)^2 = 1/3$ and $(v_s/c)^2 = 1$ and (b) the ones where p takes the values $[1.5, 2]$, while the speed of sound is parametrized in the range $(v_s/c)^2 = [1/3, 1]$.

For reasons of completeness, the treatment with both discontinuity and continuity in the speed of sound is presented in Table V of Ref. [75]. The outline was that the two approaches converge and consequently the effects of the discontinuity are negligible.

In Fig. 1 we present the pressure as a function of the rest mass density ($\rho_{\text{rest}} = n_b m_n$) and the square speed of sound in units of speed of light as a function of the transition density for the EoSs constructed in cases (a) and (b). In addition, we display the credibility intervals proposed by Ref. [24] from LIGO/Virgo collaboration for the GW170817 event. It is clear from these figures that the pure MDI-APR EoS is well-defined in the proposed limits of LIGO/Virgo collaboration and also fulfills the speed of light limit at high densities.

2.4. Structure Equations

2.4.1. Nonrotating Neutron Stars

For a static spherical symmetric system, which is the case of a nonrotating neutron star, the metric can be written as follow [1,2]

$$ds^2 = e^{\nu(r)} dt^2 - e^{\lambda(r)} dr^2 - r^2 (d\theta^2 + \sin^2 \theta d\phi^2). \quad (8)$$

The density distribution and the local pressure related to the metric functions $\lambda(r)$ and $\nu(r)$ according to the relations [1,2]

$$\frac{8\pi G}{c^2} \rho(r) = \frac{1}{r^2} (1 - e^{-\lambda(r)}) + e^{-\lambda(r)} \frac{\lambda'(r)}{r}, \quad (9)$$

$$\frac{8\pi G}{c^4} P(r) = -\frac{1}{r^2} (1 - e^{-\lambda(r)}) + e^{-\lambda(r)} \frac{\nu'(r)}{r}, \quad (10)$$

where derivatives with respect to the radius are denoted by $'$. The combination of Eqs. (9) and (10) leads to the well known Tolman-Oppenheimer-Volkoff equations [1,2]

$$\frac{dP(r)}{dr} = -\frac{G\rho(r)M(r)}{r^2} \left(1 + \frac{P(r)}{\rho(r)c^2}\right) \left(1 + \frac{4\pi P(r)r^3}{M(r)c^2}\right) \left(1 - \frac{2GM(r)}{c^2 r}\right)^{-1}, \quad (11)$$

$$\frac{dM(r)}{dr} = 4\pi r^2 \rho(r). \quad (12)$$

It is difficult to obtain exact solution of TOV equations in closed analytical form and they solved numerically with an equation of state specified [85]. Actually, there are hundreds of analytical solutions of TOV equations but there are three that satisfy the criteria that the pressure and energy density vanish on the surface of the star and also they both decrease monotonically with increasing radius. These three solutions are the Tolman VII, the Buchdahl's, and the Nariai IV. Actually, the Tolman VII and the Buchdahl's have already analyzed and

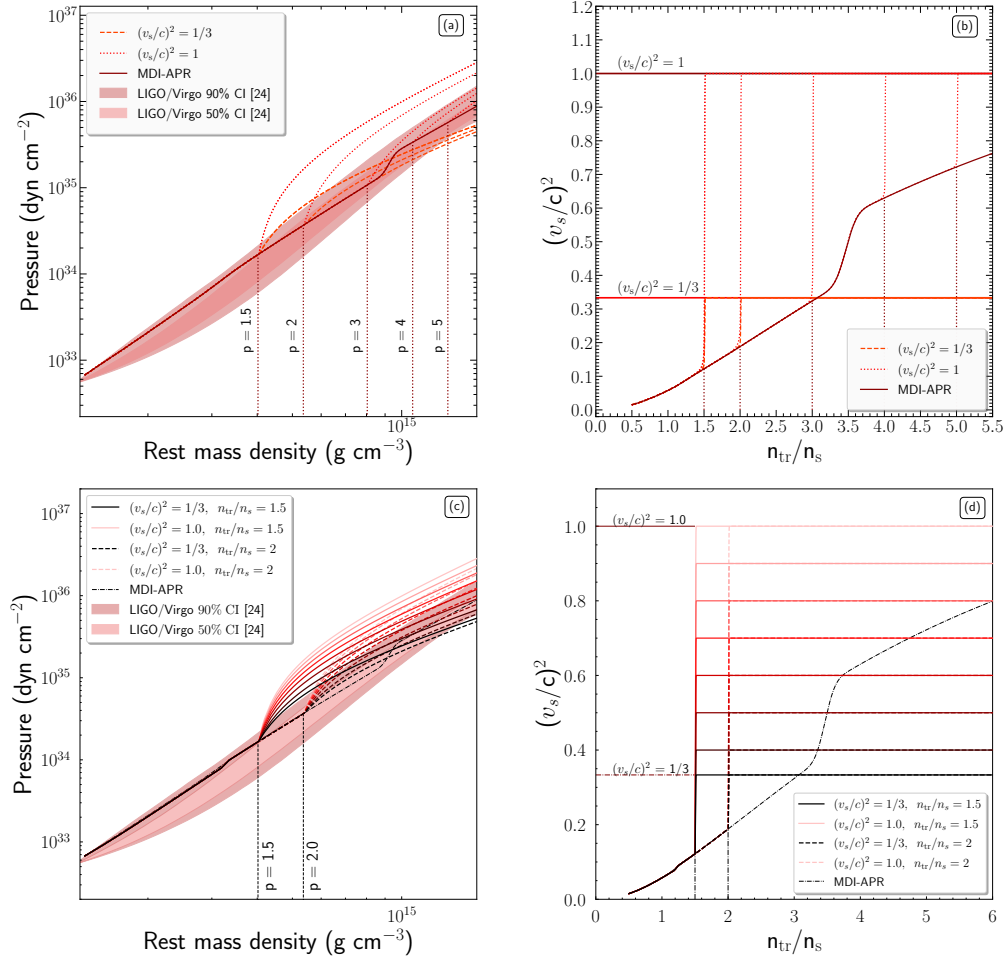


Figure 1. (a,c) Dependence of the pressure on the rest mass density and (b,d) dependence of the square sound speed in units of light speed on the transition density. (a,b) The speed of sound is fixed at the two boundary cases, $(v_s/c)^2 = 1/3$ and $(v_s/c)^2 = 1$, and the value p takes the arguments [1.5, 2, 3, 4, 5]. (c,d) The value p takes the arguments [1.5, 2], and the speed of sound is parametrized in the range $(v_s/c)^2 = [1/3, 1]$ (the lower values of the speed of sound correspond to the darker colored curves). In all Figures, the vertical dotted lines indicate the transition cases, while the shaded regions note the credibility interval derived from Ref. [24].

employed in Ref. [86]. It is worth pointing out that in the present work we use the Tolman VII solution which contains two parameters, that is the central density ρ_c and the compactness parameter $\beta = GM/Rc^2$. All the mentioned solutions have been presented and analyzed with details in Refs. [86–89].

One of the most significant sources for the terrestrial gravitational waves detectors is the gravitational waves from inspiraling binary NS systems before their merger [87,90–97]. The component masses of these binary systems can be measured. Additionally, during the last orbits before the merger, the tidal effects that are present can also be measured [91].

The dimensionless parameter that describes the response of a NS to the induced tidal field is called tidal Love number k_2 . This parameter depends on the NS structure (i.e. the mass of the neutron star, and the EoS). Specifically, the tidal Love number k_2 is a proportional parameter between the induced quadrupole moment Q_{ij} and the applied tidal field E_{ij} [91,98], given below

$$Q_{ij} = -\frac{2}{3}k_2 \frac{R^5}{G} E_{ij} \equiv -\lambda E_{ij}, \quad (13)$$

where R is the NS radius and $\lambda = 2R^5 k_2 / 3G$ is a key-role quantity, which is called tidal deformability. The tidal Love number k_2 is given by [91,92]

$$\begin{aligned} k_2 = & \frac{8\beta^5}{5}(1-2\beta)^2[2-y_R+(y_R-1)2\beta] \times \left[2\beta(6-3y_R+3\beta(5y_R-8)) \right. \\ & + 4\beta^3(13-11y_R+\beta(3y_R-2)+2\beta^2(1+y_R)) \\ & \left. + 3(1-2\beta)^2[2-y_R+2\beta(y_R-1)]\ln(1-2\beta) \right]^{-1}. \end{aligned} \quad (14)$$

The quantity y_R is determined by solving the following differential equation

$$r \frac{dy(r)}{dr} + y^2(r) + y(r)F(r) + r^2Q(r) = 0, \quad (15)$$

with the initial condition $y(0) = 2$ [94]. $F(r)$ and $Q(r)$ are functionals of $\mathcal{E}(r)$, $P(r)$ and $M(r)$ defined as [87,94]

$$F(r) = \left[1 - \frac{4\pi r^2 G}{c^4} (\mathcal{E}(r) - P(r)) \right] \left(1 - \frac{2M(r)G}{rc^2} \right)^{-1}, \quad (16)$$

and

$$\begin{aligned} r^2Q(r) = & \frac{4\pi r^2 G}{c^4} \left[5\mathcal{E}(r) + 9P(r) + \frac{\mathcal{E}(r) + P(r)}{\partial P(r)/\partial \mathcal{E}(r)} \right] \times \left(1 - \frac{2M(r)G}{rc^2} \right)^{-1} \\ & - 6 \left(1 - \frac{2M(r)G}{rc^2} \right)^{-1} - \frac{4M^2(r)G^2}{r^2 c^4} \left(1 + \frac{4\pi r^3 P(r)}{M(r)c^2} \right)^2 \left(1 - \frac{2M(r)G}{rc^2} \right)^{-2}. \end{aligned} \quad (17)$$

The Eq. (15) must be integrated self consistently combined with the TOV equations using the boundary conditions $y(0) = 2$, $P(0) = P_c$ and $M(0) = 0$ [87,92]. The numerical solution of these equations provides the mass M , the radius R of the NS, and the value of $y_R = y(R)$. The latter parameter along with the quantity β are the basic ingredients of the tidal Love number k_2 .

Moving on to the parameters of a binary NS system, a well measured quantity by the gravitational waves detectors is the chirp mass \mathcal{M}_c of the system [13,99]

$$\mathcal{M}_c = \frac{(m_1 m_2)^{3/5}}{(m_1 + m_2)^{1/5}} = m_1 \frac{q^{3/5}}{(1+q)^{1/5}}, \quad (18)$$

where m_1 is the mass of the heavier component star and m_2 is the lighter's one. Therefore, the binary mass ratio $q = m_2/m_1$ is within the range $0 \leq q \leq 1$.

Moreover, another quantity that can be constrained from the analysis of the gravitational wave signal and is of great interest is the effective tidal deformability [13,99]

$$\tilde{\Lambda} = \frac{16}{13} \frac{(12q+1)\Lambda_1 + (12+q)q^4\Lambda_2}{(1+q)^5}, \quad (19)$$

where q characterizes the mass asymmetry, and Λ_i is the dimensionless tidal deformability defined as [13,99]

$$\Lambda_i = \frac{2}{3}k_2 \left(\frac{R_i c^2}{M_i G} \right)^5 \equiv \frac{2}{3}k_2 \beta_i^{-5}, \quad i = 1, 2. \quad (20)$$

By observing Eqs. (14,20), one can find that Λ_i depends both on star's compactness and the value of $y(R)$. To be more specific, Λ_i depends directly on the stiffness of the EoS through the compactness β and indirectly through the speed of sound which appears in Eq. (17). In addition, the applied EoS affects also the behavior of Λ regarding the NS's mass M and radius R .

In our work we used the speed of sound and the transition density as parameters for stiffening the EoS, applying our study to the recent observations of both binary NS mergers and the enigmatic GW190814 event.

2.4.2. Rotating Neutron Stars

In a fully general relativistic framework, the rotating neutron stars are studied with the use of the stationary axisymmetric spacetime metric which is given by [100]

$$ds^2 = -e^{2\nu} dt^2 + e^{2\psi} (d\phi - \omega dt)^2 + e^{2\mu} (dr^2 + r^2 d\theta^2) \quad (21)$$

where the metric functions ν , ψ , ω and μ depend only on the coordinates r and θ . In order to describe a rapidly rotating neutron star, in addition to the above metric, we need the matter inside the neutron star described as a perfect fluid. By neglecting sources of non-isotropic stresses, as well as viscous ones and heat transport, then the matter inside the neutron star can be fully described by the stress-energy tensor [100],

$$T^{\alpha\beta} = (\varepsilon + P)u^\alpha u^\beta + P g^{\alpha\beta} \quad (22)$$

where u^α is the fluid's 4-velocity, and ε and P are the energy density and pressure.

For the stability of cold rotating neutron stars, the turning-point criterion is being used. It has to be noted that this is only a sufficient and not a necessary condition. Actually, the neutral stability line is positioned to the left of the turning-point line in (M, ρ_c) space, which implies that the star will collapse before reaching the turning-point line [101,102].

The numerical integration of the equilibrium equations was conducted under the RNS code [103] by Stergioulas and Friedman [104], which is actually based on the method developed by Komatsu, Eriguchi and Hachisu [105] and modifications introduced by Cook, Shapiro and Teukolsky [106].

3. Hot Neutron Stars

3.1. Thermodynamical Description of Hot Neutron Star Matter

The description of nuclear matter at finite temperature includes the Helmholtz free energy, where the differentials of the total free energy, as well as the total internal energy (assuming that the baryons are contained in volume V) are given by [107,108]

$$dF_{\text{tot}} = -S_{\text{tot}}dT - PdV + \sum_i \mu_i dN_i, \quad (23)$$

$$dE_{\text{tot}} = TdS_{\text{tot}} - PdV + \sum_i \mu_i dN_i, \quad (24)$$

where S_{tot} is the total entropy of baryons, μ_i is the chemical potential of each species, and N_i is the number of particles of each species, respectively. Furthermore, the free energy per particle can be expressed as

$$F(n, T, I) = E(n, T, I) - TS(n, T, I) = \frac{1}{n}[\mathcal{E}(n, T, I) - Ts(n, T, I)], \quad (25)$$

where $E = \mathcal{E}/n$ and $S = s/n$ are being the internal energy and entropy per particle, respectively. It has to be noted here that for $T = 0$ MeV, Eq. (25) leads to the equality between free and internal energy.

In addition, the entropy density s has the same functional form as a noninteracting gas system, calculated through the form

$$s_\tau(n, T, I) = -g \int \frac{d^3k}{(2\pi)^3} [f_\tau \ln f_\tau + (1 - f_\tau) \ln(1 - f_\tau)], \quad (26)$$

with spin degeneracy $g = [1, 2]$. The first case corresponds to protons, neutrons, electrons, and muons, and the second case, corresponds to neutrinos. Finally, the pressure and chemical potentials, which depend on the above quantities, are described as:

$$P = - \left. \frac{\partial E_{\text{tot}}}{\partial V} \right|_{S, N_i} = n^2 \left. \frac{\partial (\mathcal{E}/n)}{\partial n} \right|_{S, N_i}, \quad (27)$$

$$\mu_i = \left. \frac{\partial E_{\text{tot}}}{\partial N_i} \right|_{S, V, N_{j \neq i}} = \left. \frac{\partial \mathcal{E}}{\partial n_i} \right|_{S, V, n_{j \neq i}}. \quad (28)$$

3.2. Bulk Thermodynamic Quantities

The pressure and chemical potentials, which are essential for the thermodynamical description of nuclear matter, can also be connected to the key quantity, that is, the free energy as

$$P = - \left. \frac{\partial F_{\text{tot}}}{\partial V} \right|_{T, N_i} = n^2 \left. \frac{\partial (f/n)}{\partial n} \right|_{T, N_i}, \quad (29)$$

$$\mu_i = \left. \frac{\partial F_{\text{tot}}}{\partial N_i} \right|_{T, V, N_{j \neq i}} = \left. \frac{\partial f}{\partial n_i} \right|_{T, V, n_{j \neq i}}, \quad (30)$$

where f denotes the free energy density. It is worth mentioning that the pressure P can also be determined by [107,108],

$$P = Ts - \mathcal{E} + \sum_i \mu_i n_i. \quad (31)$$

In this case, the calculation of the entropy per particle is possible by differentiating the free energy density f with respect to the temperature,

$$S(n, T) = - \left. \frac{\partial (f/n)}{\partial T} \right|_{V, N_i} = - \left. \frac{\partial F}{\partial T} \right|_n. \quad (32)$$

By applying Eq. (30), the chemical potentials take the form [37,109,110]

$$\mu_n = F + u \left. \frac{\partial F}{\partial u} \right|_{Y_p, T} - Y_p \left. \frac{\partial F}{\partial Y_p} \right|_{n, T}, \quad (33)$$

$$\mu_p = \mu_n + \left. \frac{\partial F}{\partial Y_p} \right|_{n, T}, \quad (34)$$

$$\hat{\mu} = \mu_n - \mu_p = - \left. \frac{\partial F}{\partial Y_p} \right|_{n, T}. \quad (35)$$

The free energy $F(n, T, I)$ and the internal energy $E(n, T, I)$, as well as the entropy which depends on the latter quantities, can have the following quadratic dependence from the asymmetry parameter [37,110–113]:

$$F(n, T, I) = F(n, T, I = 0) + I^2 F_{\text{sym}}(n, T), \quad (36)$$

$$E(n, T, I) = E(n, T, I = 0) + I^2 E_{\text{sym}}(n, T), \quad (37)$$

$$S(n, T, I) = S(n, T, I = 0) + I^2 S_{\text{sym}}(n, T), \quad (38)$$

as the parabolic approximation (PA) suggests, where

$$F_{\text{sym}}(n, T) = F(n, T, I = 1) - F(n, T, I = 0), \quad (39)$$

$$E_{\text{sym}}(n, T) = E(n, T, I = 1) - E(n, T, I = 0), \quad (40)$$

$$S_{\text{sym}}(n, T) = S(n, T, I = 1) - S(n, T, I = 0) = \frac{1}{T} (E_{\text{sym}}(n, T) - F_{\text{sym}}(n, T)). \quad (41)$$

While the above approximation is valid for the specific model, in general, its checking is mandatory. For completeness, the PA is satisfied in both the internal energy and the free energy as Refs. [37,110–113] state. However, there are studies [114] in which the PA contains uncertainties. By concluding, the PA and its validity strongly depend on the specific character of the selected nuclear model.

Eq. (35), which is mandatory for this approximation, can be acquired by substituting Eq. (36) as

$$\hat{\mu} = \mu_n - \mu_p = 4(1 - 2Y_p)F_{\text{sym}}(n, T). \quad (42)$$

This equation is similar to that obtained for cold catalyzed nuclear matter by replacing $E_{\text{sym}}(n)$ with $F_{\text{sym}}(n, T)$.

3.3. Lepton's Contribution

Stable nuclear matter and chemical equilibrium state is explicitly connected at high densities for all reactions, Stable nuclear matter at high densities requires a chemical equilibrium state for all reactions, Specifically, electron capture and β decay take place simultaneously

$$p + e^- \longrightarrow n + \nu_e, \text{ and } n \longrightarrow p + e^- + \bar{\nu}_e. \quad (43)$$

In consequence, a change in the electron fraction Y_e is in order. Considering that the generated neutrinos have left the system, a significant effect on the EoS is presented by changing the values of proton fraction Y_p [115,116]. In particular, the absence of neutrinos implies that

$$\hat{\mu} = \mu_n - \mu_p = \mu_e. \quad (44)$$

It has to be mentioned that, in principle, the matter contains neutrons, protons, electrons, muons, photons, and antiparticles, which are in a thermal equilibrium state. However, in the present study we consider only the contribution of neutron, protons, and electrons, as the contribution of the remaining particles is negligible [115]. As a consequence, the following relation holds:

$$\mu_n = \mu_p + \mu_e. \quad (45)$$

The energy density and pressure of leptons are calculated through the following formulae:

$$\mathcal{E}_l(n_l, T) = \frac{2}{(2\pi)^3} \int \frac{d^3k \sqrt{\hbar^2 k^2 c^2 + m_l^2 c^4}}{1 + \exp\left[\frac{\sqrt{\hbar^2 k^2 c^2 + m_l^2 c^4} - \mu_l}{T}\right]}, \quad (46)$$

$$P_l(n_l, T) = \frac{1}{3} \frac{2(\hbar c)^2}{(2\pi)^3} \int \frac{1}{\sqrt{\hbar^2 k^2 c^2 + m_l^2 c^4}} \times \frac{d^3k k^2}{1 + \exp\left[\frac{\sqrt{\hbar^2 k^2 c^2 + m_l^2 c^4} - \mu_l}{T}\right]}. \quad (47)$$

The chemical potential of electrons is available through the Eqs. (42) and (45), as

$$\mu_e = \mu_n - \mu_p = 4I(n, T)F_{\text{sym}}(n, T). \quad (48)$$

which is crucial for the calculation of the proton fraction as a function of both the baryon density and the temperature. The construction of the EoS of hot nuclear matter in the β -equilibrium state is provided through the calculation of the total energy density \mathcal{E}_t , as well as the total pressure P_t . The total energy density (with all terms) is given by

$$\mathcal{E}_t(n, T, I) = \mathcal{E}_b(n, T, I) + \sum_l \mathcal{E}_l(n, T, I) + \sum_{\bar{l}} \mathcal{E}_{\bar{l}}(n, T, I) + \mathcal{E}_\gamma(n, T), \quad (49)$$

where $\mathcal{E}_b(n, T, I)$ is the contribution of baryons, $\mathcal{E}_l(n, T, I)$, $\mathcal{E}_{\bar{l}}(n, T, I)$ are the contributions of particles and antiparticles of leptons, and $\mathcal{E}_\gamma(n, T)$ is the contribution of photons. The total pressure (with all terms) is

$$P_t(n, T, I) = P_b(n, T, I) + \sum_l P_l(n, T, I) + \sum_{\bar{l}} P_{\bar{l}}(n, T, I) + P_\gamma(T), \quad (50)$$

where $P_b(n, T, I)$ is the contribution of baryons,

$$P_b(n, T, I) = T \sum_{\tau=p,n} s_\tau(n, T, I) + \sum_{\tau=n,p} n_\tau \mu_\tau(n, T, I) - \mathcal{E}_b(n, T, I), \quad (51)$$

while $P_l(n, T, I)$, $P_{\bar{l}}(n, T, I)$ are the contributions of particles and antiparticles of leptons, and $P_\gamma(T)$ is the contribution of photons.

3.4. Isothermal Configuration

In the isothermal temperature profile, by considering that for each value of temperature, the value of the proton fraction is a well-known function of the baryon density, the total energy density is evaluated as

$$\mathcal{E}_t(n, T, Y_p) = \mathcal{E}_b(n, T, Y_p) + \mathcal{E}_e(n, T, Y_p), \quad (52)$$

where

$$\mathcal{E}_b(n, T, Y_p) = nF_{\text{PA}} + nTS_{\text{PA}}, \quad (53)$$

$\mathcal{E}_e(n, T, Y_p)$ is given by Eq. (46) replacing the leptons with electrons and μ_e from Eq. (48), and F_{PA} and S_{PA} are given by Eqs. (36) and (38), respectively. Moreover, the total pressure is evaluated as

$$P_t(n, T, Y_p) = P_b(n, T, Y_p) + P_e(n, T, Y_p), \quad (54)$$

where

$$P_b(n, T, Y_p) = n^2 \left. \frac{\partial F_{\text{PA}}(n, T, Y_p)}{\partial n} \right|_{T, n_i}, \quad (55)$$

and $P_e(n, T, Y_p)$ is given by Eq. (46) replacing the leptons with the electrons and μ_e from Eq. (48).

Thus, the Eqs. (52) and (54) for the energy density and the pressure, respectively, correspond to the ingredients for the construction of isothermal EoSs of hot nuclear matter in β equilibrium state.

3.5. Isentropic Configuration and Neutrino Trapping

In isentropic configuration we assume that the entropy per baryon and lepton fraction are constant in the interior of the neutron star (protoneutron star). Specifically, according to Eq. (43), the neutrinos are trapped in the interior of the star and the proton fraction is significantly increased. The relevant chemical equilibrium can be expressed in terms of the chemical potentials for the four species,

$$\mu_n + \mu_{\nu_e} = \mu_p + \mu_e. \quad (56)$$

In addition, the charge neutrality demands the equality between proton and electron fraction, while the total fraction of leptons is equal to $Y_l = Y_e + Y_{\nu_e}$. Henceforth, the chemical equilibrium is expressed as

$$\mu_e - \mu_{\nu_e} = \mu_n - \mu_p = 4(1 - 2Y_p)F_{\text{sym}}(n, T). \quad (57)$$

In this case too, the relevant system of equations can provide us with the density and temperature dependence of proton and neutrino fractions, and their chemical potentials, by assuming a constant entropy per baryon. Nonetheless, we applied the approximation of $Y_p \simeq 2/3Y_l + 0.05$ (3% accuracy) introduced by Takatsuka *et al.* [115], in order to avoid computational complications. The ingredients for the construction of isentropic EoSs are given by the Eqs. (49) and (50).

3.6. Construction of the Hot EoSs

The construction of the EoS for the interior of neutron stars at finite temperature and entropy per baryon is based on the MDI model and data provided by Akmal *et al.* [74]. In particular, we utilized the APR-1 EoS data from Akmal *et al.* [74] for the energy per particle of SNM and PNM in the density range $[0.04, 0.96] \text{ fm}^{-3}$. The process lead to the evaluation of the coefficients for the symmetric and asymmetric nuclear matter, and finally, to the construction of the EoS, hereafter MDI+APR1.

In the case of the isothermal temperature profile, we have constructed 10 EoSs in the temperature range $[1, 60] \text{ MeV}$, while in the isentropic case, we have constructed nine EoSs in entropy per baryon and lepton fraction in the ranges $[1, 3] k_B$ and $[0.2, 0.4]$, respectively. For the crust region of the finite temperature cases and the low-density region ($n_b \leq 0.08 \text{ fm}^{-3}$), as well as the finite entropies per baryon and lepton fractions, the EOSs of Lattimer and

Swesty [30] and the specific model corresponding to the incomprehensibility modulus at the saturation density of SNM $K_s = 220$ MeV are used (<https://www.stellarcollapse.org>).

3.7. Rapidly Rotating Hot Neutron Stars

The stability of hot neutron stars is acquired via a specific version of the secular instability criterion of Friedman *et al.* [117], which follows Theorem I of Sorkin [118]. In a continuous sequence of equilibria at a fixed baryon number N_{bar} and total entropy of the neutron star S_t^{ns} , the extremal point of the stability loss is found when [119]

$$\left. \frac{\partial J}{\partial n_b^c} \right|_{N_{\text{bar}}, S_t^{\text{ns}}} = 0, \quad (58)$$

where J and n_b^c are the angular momentum and central baryon density of the star, respectively.

Furthermore, in a sequence the turning-point appears in the case where three out of four following derivatives,

$$\frac{\partial M_{\text{gr}}}{\partial n_b^c}, \quad \frac{\partial M_b}{\partial n_b^c}, \quad \frac{\partial J}{\partial n_b^c}, \quad \text{and} \quad \frac{\partial S_t^{\text{ns}}}{\partial n_b^c}, \quad (59)$$

where M_{gr} and M_b denote the gravitational and baryon mass, vanish [52,120]. In addition, the turning-point theorem shows that at this point, the fourth derivative also vanishes, and the sequence has transitioned from stable to unstable.

It has to be mentioned that the criterion for secularly stable/unstable configurations is essential only for constant entropy per baryon or temperature [120]. In this review, the entropy per baryon, as well as the temperature, in each case respectively, are constant throughout the neutron star. As a consequence, the remaining criteria vanish at the maximum mass configuration (last stable point). Furthermore, we considered that in the rotating configuration, the maximum mass and the maximum angular velocity coincide, which generally is not the case [100]. However, the existed difference is very small, and it could not be detected within the precision of our calculations [119].

The numerical integration of the equilibrium equations was conducted under the publicly available numerical code *nrotstar* from the C++ Lorene/Nrotstar library [121].

4. Results and Discussion

4.1. Speed of Sound and Tidal Deformability

In our study we used two cases for the value of speed of sound, the lower bound of $(v_s/c)^2 = 1/3$ and the upper one of $(v_s/c)^2 = 1$, and four transition densities $n_{\text{tr}} = \{1, 1.5, 2, 3\}n_0$ [65].

In Fig. 2 we display the corresponding mass-radius (M-R) diagram which we obtained from the numerical solution of the TOV system of equations. The green colored lines correspond to the $(v_s/c)^2 = 1/3$ limit, while the blue ones correspond to the $(v_s/c)^2 = 1$ limit. One can observe that each transition density leads to bifurcations in the M-R diagram. Between the same kind of linestyle, the lower (upper) bound $(v_s/c)^2 = 1/3$ ($(v_s/c)^2 = 1$) of speed of sound corresponds to lower (higher) masses. In general, the higher the transition density, the softer the EoS, with the lower bound of $(v_s/c)^2 = 1/3$ leading to a more soft EoS, compare to the $(v_s/c)^2 = 1$ case. In addition, the estimation of the GW170817 event and the NICER's data are also displayed [24,122]. We notice that while there is an accordance between the two observations, the GW170817 event (from the gravitational-waves perspective) is more informative for our study than the NICER's detection, as it restricts the cases leading to the exclusion of EoS at least with transition density $n_{\text{tr}} = n_0$, for both bounds of speed of sound.

Our study takes into consideration the observation of binary neutron stars mergers from the gravitational waves detectors. Therefore, we used the measured upper limit of the effective

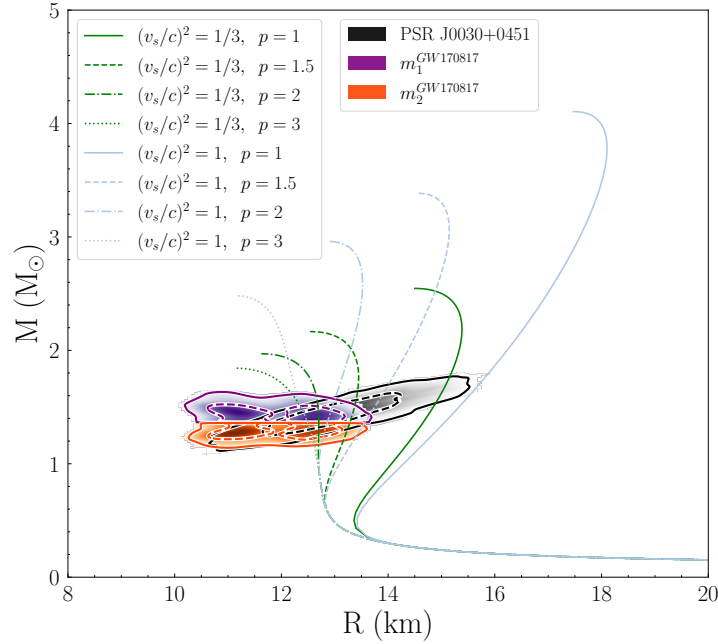


Figure 2. Mass vs radius for an isolated neutron star, and for the two cases of speed of sound bounds. The blue (green) lines correspond to the upper (lower) bound. The black diagonal shaded region corresponds to NICER's observation (data taken from Ref. [122]), while the purple upper (orange lower) shaded region corresponds to the higher (smaller) component of GW170817 event (data taken from Ref. [24]). The solid (dashed) contour lines describe the 90% (50%) confidence interval.

tidal deformability $\tilde{\Lambda}$, provided by the events GW170817 and GW190425 [14,24,99]. The chirp masses for the two events are $\mathcal{M}_c = 1.186 M_\odot$ [13] and $\mathcal{M}_c = 1.44 M_\odot$ [14], respectively. The component masses vary in the ranges $m_1 \in (1.36, 1.60) M_\odot$ and $m_2 \in (1.16, 1.36) M_\odot$ [99] (GW170817) and $m_1 \in (1.654, 1.894) M_\odot$ and $m_2 \in (1.45, 1.654) M_\odot$ (GW190425). We notice that we modified the range of the component masses (especially in the second event) to have an equal-mass boundary, i.e. $q \leq 1$.

In Fig. 3 we display the effective tidal deformability $\tilde{\Lambda}$ as a function of q for both events. In Fig. 3(a), we observe that the upper limit on $\tilde{\Lambda}$ (derived from the GW170817 event), leads to the exclusion of both cases of speed of sound with transition density $n_{\text{tr}} = 1, 1.5 n_0$. By comparing to Fig. 2, the constraints on the upper limit of $\tilde{\Lambda}$ in the Fig. 3 make more clear which cases must be excluded. For the second event in Fig. 3(b), we observe that all the EoSs are shifted to lower values of $\tilde{\Lambda}$, compared to the GW170817 event. This is because of the higher value of chirp mass in the second event (GW190425). Contrary to the GW170817 event, the upper limit on $\tilde{\Lambda}$, provided by GW190425 event excludes only these EoSs with transition density $n_{\text{tr}} = n_0$, for both speed of sound bounds. In general, for both events, the EoSs corresponding to higher values of transition density n_{tr} lead to smaller values of $\tilde{\Lambda}$. Therefore, the measured upper limits of $\tilde{\Lambda}$ favor softer EoSs. We have to notice that for the GW190425 event, we did not take into consideration the cases with transition density $n_{\text{tr}} = 3 n_0$ because the EoS with $(v_s/c)^2 = 1/3$ and $n_{\text{tr}} = 3 n_0$ can not reproduce the masses of this event.

Beyond the useful constraints that we obtained so far by the study of the EoSs through the observed upper limit of $\tilde{\Lambda}$, a more direct connection between this quantity and the speed of sound bounds is still needed. This idea that lies at the very heart of our study was the main motive. Such a direct relation between the referred quantities can be accomplished if we treat

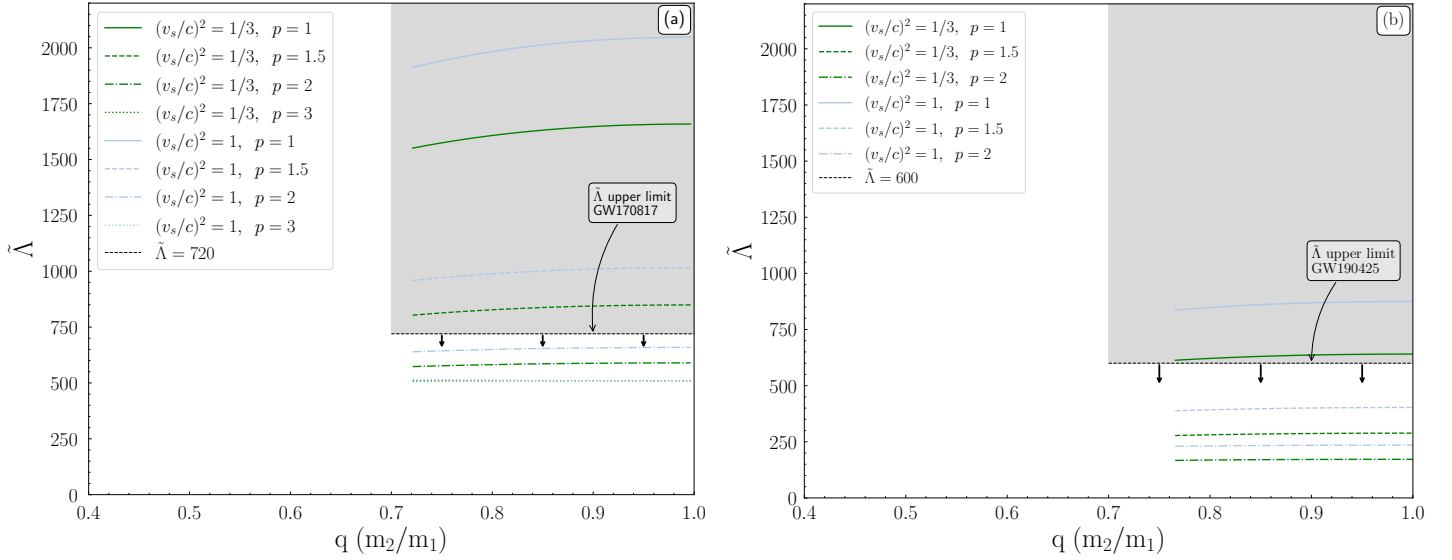


Figure 3. The effective tidal deformability $\tilde{\Lambda}$ as a function of the binary mass ratio q for the event (a) GW170817 and (b) GW190425. The measured upper limits for $\tilde{\Lambda}$ are also indicated, with the grey shaded region corresponding to the excluded area. The green (blue) curves correspond to the $(v_s/c)^2 = 1/3$ ($(v_s/c)^2 = 1$) case.

the variation of $\tilde{\Lambda}$ in Fig. 3 as a function of the transition density n_{tr} , i.e. the $\tilde{\Lambda}_{\text{min}}^{(1/3,1)} - n_{\text{tr}}$ and $\tilde{\Lambda}_{\text{max}}^{(1/3,1)} - n_{\text{tr}}$ relations.

In Fig. 4 we display the relation between the effective tidal deformability $\tilde{\Lambda}$ and the transition density n_{tr} at the maximum mass configuration for the two speed of sound bounds, $v_s = c/\sqrt{3}$ and $v_s = c$, and the two events GW170817 (Fig. 4(a)) and GW190425 (Fig. 4(b)). The corresponding upper measured limits for $\tilde{\Lambda}$, as well as the compatible lower transition density values, are also indicated. The predictions on the bound of the speed of sound which are considered between the two referred limits correspond to the middle region.

The main remarks from the observation of Fig. 4 are the following

1. The overall thickness decreases as the transition density n_{tr} getting higher values. This behavior can be explained by the variation of the radius $M(R)$ presented with the M-R diagram (see Fig. 2).
2. The thickness of each shaded region decreases as the n_{tr} gets higher values.
3. The shaded areas are shifted downwards in the GW190425 event, compared with the GW170817 event. This behavior is because of due to the increment of the component masses. A similar behavior was observed in Fig. 3(b), compared to Fig. 3(a).

According to our findings, for the GW170817 event the lower limit for the transition density is $1.626n_0$ for $v_s = c/\sqrt{3}$ and $1.805n_0$ for $v_s = c$. In the case of the second event GW190425, the corresponding limits are $1.015n_0$ for $v_s = c/\sqrt{3}$ and $1.216n_0$ for $v_s = c$. Therefore, the first event imposes more stringent constraints on the EoS. In particular, the value of the speed of sound must be lower than $v_s = c/\sqrt{3}$, at least up to density $1.626n_0$ (so the EoS is soft enough to predict the tidal deformability). Furthermore, the EoS must remain casual at least up to density $1.805n_0$. In addition, according to the Fermi liquid theory (FLT) the speed of sound must be $v_{s,\text{FLT}}^2 \leq 0.163c^2$ for $n = 1.5n_0$ [123], meaning that the EoS cannot exceed this value for $n \leq 1.5n_0$, which is in agreement with our finding of the lower limit $n_{\text{tr}} = 1.626n_0$ for the case of $v_s = c/\sqrt{3}$.

We notice that so far we used the upper limit on $\tilde{\Lambda}$ to impose stringent constraints on the n_{tr} . The existence of a lower limit on $\tilde{\Lambda}$ could provide further information. Indeed, for the

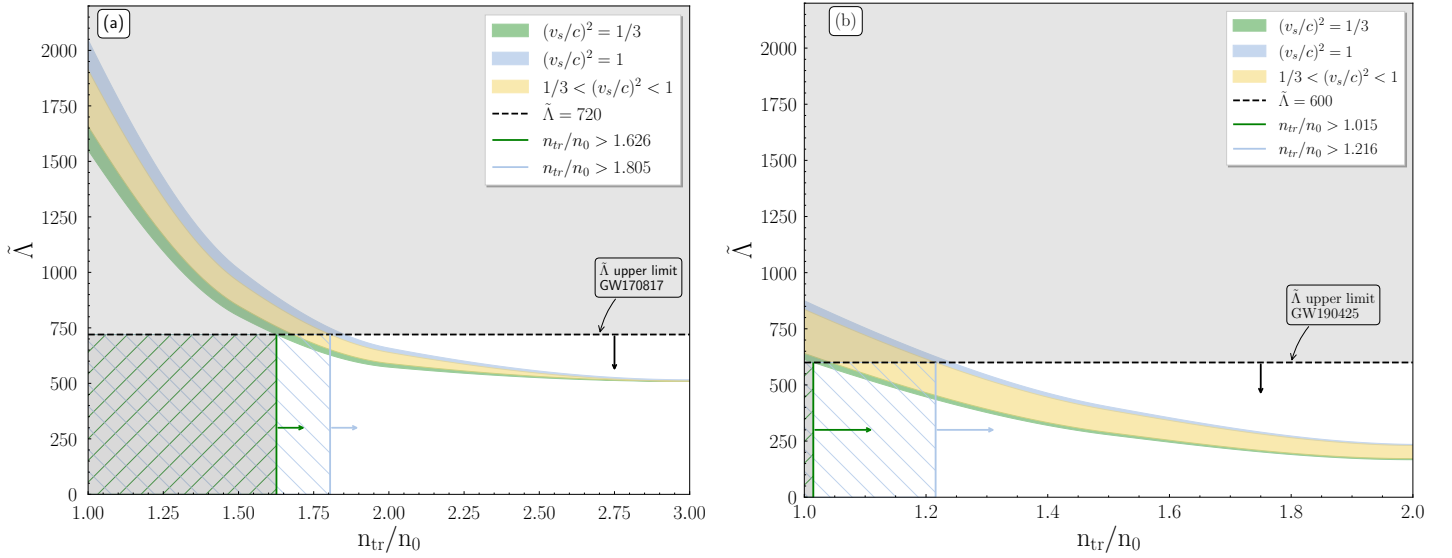


Figure 4. $\tilde{\Lambda}$ as a function of the transition density n_{tr} (in units of saturation density n_0) at the maximum mass configuration for the two speed of sound bounds $v_s = c/\sqrt{3}$ and $v_s = c$ and for the event (a) GW170817 and (b) GW190425. The measured upper limits for $\tilde{\Lambda}$ [14,99] as well as the corresponding lower values of transition density are also indicated for both events. The green (blue) arrow marks the accepted region of transition density for the $v_s = c/\sqrt{3}$ ($v_s = c$) case. The green lower (blue upper) curved shaded region corresponds to the $v_s = c/\sqrt{3}$ ($v_s = c$) limit. The yellow shaded area indicates the region between the two cases of speed of sound bounds.

GW170817 event such a lower limit is provided both by the gravitational wave data [24,99] and the electromagnetic (EM) counterpart of the merger [124–129]. Most *et al.* [130] used the bound of Ref. [124] and demonstrated its significance in order to constrain further the tidal deformability $\tilde{\Lambda}_{1.4}$ and the radius $R_{1.4}$ of a $M = 1.4 M_\odot$ neutron star. For our case of interest and especially for the GW170817 event, a lower limit on $\tilde{\Lambda}$, similar to the proposed values, could not provide any further constraint, even if we consider the more optimistic boundary of $\tilde{\Lambda} \geq 400$.

On the contrary, for the second event GW190425, its higher component masses lead to smaller values on $\tilde{\Lambda}$. Hence, there is an inability for the upper limit of $\tilde{\Lambda}$ to provide further constraints. We speculate that the existence of a lower limit on $\tilde{\Lambda}$ would be able to provide constraints, especially leading to an upper limit for n_{tr} . Hence, binary neutron stars coalescences with heavy masses would be helpful to constrain the upper limit of n_{tr} via the lower limit of $\tilde{\Lambda}$ as provided by the EM counterpart. Unfortunately, an EM counterpart for the GW190425 event was not detected [14,131].

Furthermore, we provide in Fig. 4 an expression for the $\tilde{\Lambda}_{\min}^{(1/3)}$ and $\tilde{\Lambda}_{\min}^{(1)}$ boundary curves of the green (lower) and blue (upper) shaded regions, respectively. This expression gives the exact value of the lower limit on $n_{tr}^{(1/3)}$ and $n_{tr}^{(1)}$, respectively. The expression is given by the following equation, and the coefficients on the Table 1,

$$\tilde{\Lambda} = c_1 \coth \left[c_2 \left(\frac{n_{tr}}{n_0} \right)^2 \right]. \quad (60)$$

As one can observe from Fig. 2, the highest mass is provided by the stiffest EoSs, i.e. the higher value of speed of sound. Therefore, the behavior of the maximum mass M_{\max} and the speed of sound v_s^2 has to be studied further.

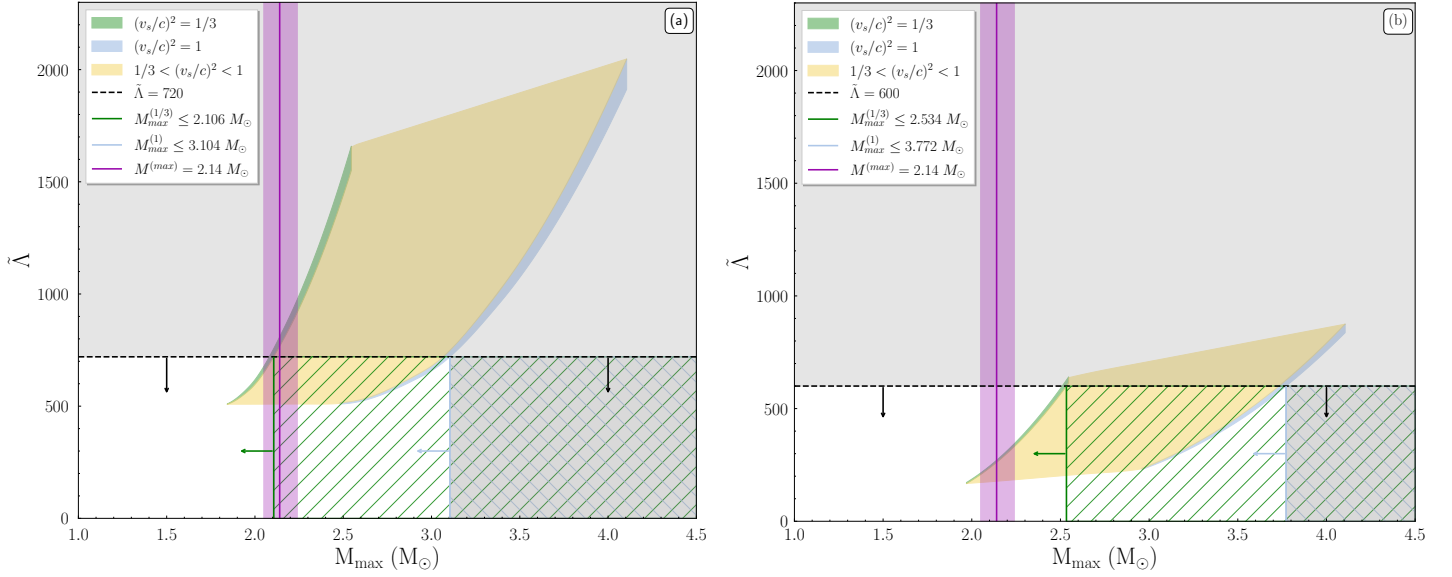


Figure 5. The effective tidal deformability $\tilde{\Lambda}$ as a function of the maximum mass for the two speed of sound bounds $v_s = c/\sqrt{3}$ and $v_s = c$ and for the event (a) GW170817 and (b) GW190425. The measured upper limits for $\tilde{\Lambda}$ (black dashed lines with arrows, see Refs. [14,99]), the corresponding maximum mass shaded regions, for $v_s = c/\sqrt{3}$ (left green) case, $v_s = c$ case (right blue) and the middle cases (yellow), as well the current observed maximum neutron star mass $M = 2.14^{+0.10}_{-0.09} M_\odot$ (purple shaded vertical area, see Ref. [17]) are also displayed. The green left (blue right) arrow marks the accepted region of maximum mass M_{\max} for $v_s = c/\sqrt{3}$ ($v_s = c$) case.

In Fig. 5 the behavior of the effective tidal deformability $\tilde{\Lambda}$ as a function of the maximum mass for the two speed of sound bounds and for both events, is displayed. The corresponding upper observational limit for $\tilde{\Lambda}$ (black dashed horizontal line), the compatible maximum mass in each case (horizontal arrows), as well as the current observed maximum neutron star mass $M = 2.14^{+0.10}_{-0.09} M_\odot$ (vertical purple shaded region) are also indicated.

At first glance in Fig. 5, there is a contradiction between the maximum mass and the upper limit of the observed $\tilde{\Lambda}$. For the first event in Fig. 5(a), the upper limit of $\tilde{\Lambda}$ is compatible with a maximum mass value $2.106 M_\odot$ for $v_s = c/\sqrt{3}$ and $3.104 M_\odot$ for $v_s = c$. Nonetheless, this bound corresponds to transition density in approximation $1.5n_0$. Experimental evidences disfavor this value. Therefore, the simultaneously derivation of the maximum mass combined with the experimental knowledge that the EoS cannot take this bound of sound speed for $n_{\text{tr}} = 1.5n_0$, are in contradiction. Furthermore, the upper limit on M_{\max} for the case of $(v_s/c)^2 = 1/3$ lays roughly inside the estimation of the measured maximum mass. In the general perspective, we notice that two different points of view antagonize each other. The constraints derived by the upper limit on $\tilde{\Lambda}$ lead to softer EoSs, contrary to the observational estimations of the maximum mass of neutron stars which lead to stiffer EoSs. As we move to higher values of the speed of sound, this contrast decreases, with the causal scenario of $v_s = c$ leading to a very wide area for the maximum mass.

In the case of the second event GW190425 displayed in Fig. 5(b), the constraints provided by the measured $\tilde{\Lambda}$ are less stringent than the GW170817 event, with a maximum mass value of $M_{\max} \leq 2.534 M_\odot$ for $v_s = c/\sqrt{3}$ and $M_{\max} \leq 3.772 M_\odot$ for $v_s = c$. Although, the presence of a lower limit on $\tilde{\Lambda}$, especially in the case of events with heavy components (such as GW190425), could constrain the lower maximum mass.

In addition, we provide an expression that describes the $\tilde{\Lambda}$ as a function of the maximum mass M_{max} . The expression is given by the following equation and the coefficients on the Table 1,

$$\tilde{\Lambda} = c_3 \left(e^{M_{\text{max}}} - 1 \right)^{c_4}. \quad (61)$$

The expression in this form means that when $M_{\text{max}} \rightarrow 0 \Rightarrow \tilde{\Lambda} \rightarrow 0$. Moreover, the adoption of an upper limit on the maximum mass M_{max} in Fig. 5, could provide an additional constraint on the behavior of the speed of sound. Specifically, by applying the estimated upper limit $M_{\text{max}} \leq 2.33 M_{\odot}$ [132], the case of $(v_s/c)^2 = 1$ in Fig. 5(a) for the GW170817 event should be excluded. On the contrary, the estimated upper limit $M_{\text{max}} \leq 2.106 M_{\odot}$ for the $(v_s/c)^2 = 1/3$ bound, is a more tight constrain. Additionally, an upper limit such as $M_{\text{max}} \leq 2.33 M_{\odot}$ imposes a general upper bound on the possible intermediate values of speed of sound (intermediate shaded area in the figure). Concerning the second event in Fig. 5(b), a strict upper limit on M_{max} could constrain even the $(v_s/c)^2 = 1/3$ case.

Table 1. Parameters of the Equation (60) and Equation (61) for both events and all speed of sound bounds.

| Bounds | GW170817 | | | | GW190425 | | | |
|--------------|----------|-------|--------|-------|----------|-------|--------|-------|
| | c_1 | c_2 | c_3 | c_4 | c_1 | c_2 | c_3 | c_4 |
| c | 500.835 | 0.258 | 53.457 | 0.873 | 47.821 | 0.055 | 10.651 | 1.068 |
| $c/\sqrt{3}$ | 503.115 | 0.325 | 38.991 | 1.493 | 43.195 | 0.069 | 5.024 | 1.950 |

Another interesting relation is the $\tilde{\Lambda}$ as a function of the radius of a $1.4 M_{\odot}$ neutron star, for both events, which is displayed in Fig. 6. First of all, the upper limit on $\tilde{\Lambda}$ leads to a limitation on the maximum values of the radius, especially in the case of $v_s = c/\sqrt{3}$. Also, there is a trend between $\tilde{\Lambda}$ and $R_{1.4}$, which was remarked also by Raithel *et al.* [133], mentioning that the effective tidal deformability depends strongly on the radii of the stars rather on the component masses. This strong dependence can be observed in Fig. 6.

In particular, for the GW170817 event the curves of the two limited cases, red (blue) for the $(v_s/c)^2 = 1/3$ ($(v_s/c)^2 = 1$) bound of the speed of sound, are almost identical. The cross marks correspond to the specific values for each case. In our study we considered 4 cases of transition density n_{tr} , therefore 8 marks are expected totally, but in the diagram, they can be seen only 7 marks. This is because of the identical values for the $n_{\text{tr}} = 3n_0$ case that the two bounds provide. This is clear from their behavior in Fig. 2 in which, for the mass range of GW170817 event, their M-R curves are identical.

Moreover, as the effective tidal deformability $\tilde{\Lambda}$ is getting higher values, the distance between them also increases. The same behavior is present in the curves of Fig. 3(a), in which their in-between distance increases for higher values of $\tilde{\Lambda}$. This increment is related to the n_{tr} , meaning that the differentiation for small values of n_{tr} is more obvious. Hence, in these cases the effect of each bound of the speed of sound is easier to be manifested.

The dotted purple line corresponds the approximate relation of Refs. [134,135]. We notice that this approximate relation is valid only for the first event and for specific assumptions on the components' radii. Especially, the main assumption of this approximation consists on the $R_1 \approx R_2$ relation. From the comparison of Fig. 6 to the M-R diagram of Fig 2, it follows that for smaller values of n_{tr} (i.e. more stiff EoSs), (a) the inclination of the curves increases and (b) the difference between the M-R curves of boundary cases is also increases. Therefore, these remarks combined with the strong dependence of Λ_i to R (see Eq. (20)), the inability of the proposed expression to reproduce accurately the values of $\tilde{\Lambda}$ in the high-values region can be explained.

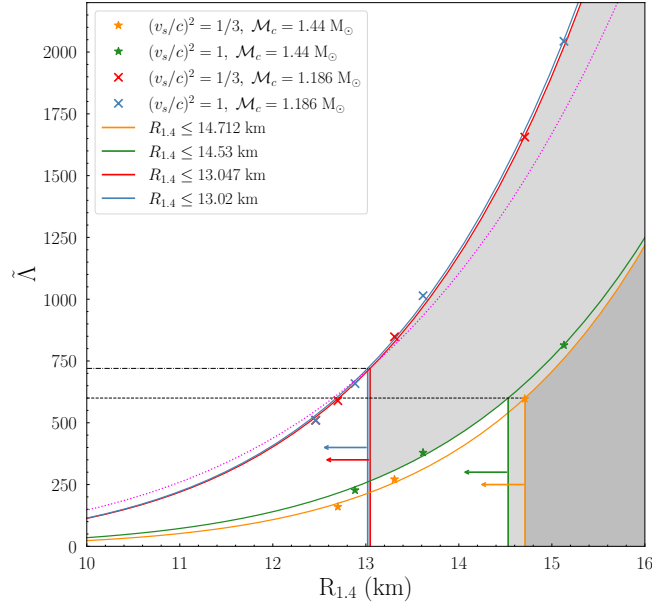


Figure 6. The effective tidal deformability $\tilde{\Lambda}$ as a function of $R_{1.4}$ for both events and all the bounds of speed of sound. The dashed (dashdotted) horizontal black line corresponds to the upper limit on $\tilde{\Lambda}$ for GW190425 (GW170817) event, taken from Refs. [14,99]. The grey shaded regions corresponds the excluded areas. The horizontal arrows indicate the allowed area for $R_{1.4}$ in each case. The purple dotted curve demonstrates the proposed expression by Refs. [134,135].

The grey shaded area indicates the excluded area due to the upper limit on $\tilde{\Lambda}$, provided by Ref. [99]. The upper limit of $\tilde{\Lambda}$ leads to constraints on the radius $R_{1.4}$, especially $R_{1.4} \leq 13.047$ km for $(v_s/c)^2 = 1/3$ bound and $R_{1.4} \leq 13.02$ km for $(v_s/c)^2 = 1$ bound. These upper limits are consistent to other analyses [24,125,129,130,133,135–138].

For the second event (GW190425), we notice that the exact range of the component masses is not determinant [131]. The orange (green) lines and marks correspond to the $(v_s/c)^2 = 1/3$ ($(v_s/c)^2 = 1$) speed of sound bound. The shaded grey region indicates the excluded region by the upper limit of $\tilde{\Lambda}$ [14]. The orange and green arrows indicate the allowed region for each case. For $(v_s/c)^2 = 1/3$ the constraint on the radius is $R_{1.4} \leq 14.712$ km, while for $(v_s/c)^2 = 1$ is $R_{1.4} \leq 14.53$ km. These are more stringent constraints compared to the 15 km and 16 km of Ref. [14]. We notice that recently it was found in Ref. [139] that the joint contribution of gravitational wave and NICER data favors the violation of the conformal limit $(v_s/c)^2 < 1/3$. Especially, this analysis suggest the violation of the conformal limit around $4\rho_{\text{nuc}}$ density, where $\rho_{\text{nuc}} = 2.8 \times 10^{14} \text{ g/cm}^3$ is the nuclear saturation density.

In addition, one can observe the similarity of the curves' behavior between the two events. For higher values of n_{tr} the distance between the points is getting bigger. One of the main difference is that for the second event, the curves and the points have been shifted to smaller values of $\tilde{\Lambda}$ because of the higher chirp mass \mathcal{M}_c of the system. Another observation is that the fitting lines are more distinct from each other, contrary to the GW170817 event in which they were almost identical; nevertheless, there is a common trend (see also Ref. [133]). For this reason, we applied the expression, that is similar to the proposed relations of Refs. [134,135],

$$\tilde{\Lambda} = c_1 R_{1.4}^{c_2}, \quad (62)$$

where $R_{1.4}$ is in km. The coefficients for each case are given in Table 2.

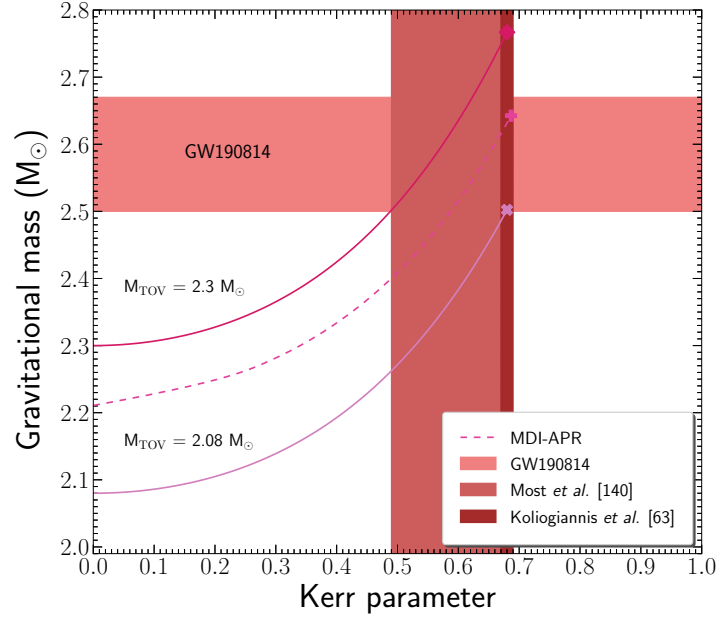


Figure 7. Dependence of the gravitational mass on the Kerr parameter. The lower solid line represents the Eq. (63) with $M_{\text{TOV}} = 2.08 M_{\odot}$, while the upper solid line represents the Eq. (63) with $M_{\text{TOV}} = 2.3 M_{\odot}$. The dashed line corresponds to the MDI-APR EoS. In addition, the horizontal shaded region notes the mass of the second component of GW190814 event and the vertical wide shaded region, marks the Kerr parameter, $\mathcal{K} = [0.49, 0.68]$, according to Ref. [140]. Furthermore, the narrow vertical shaded region indicates the Kerr parameter, $\mathcal{K}_{\text{max}} = [0.67, 0.69]$, extracted from Ref. [63] by assuming that the low mass component was rotating at its mass-shedding limit. The cross, the plus sign, and the diamond point the maximum mass configuration at the mass-shedding limit.

Table 2. Coefficients of Equation (62) for the two speed of sound bounds.

| Event | Bounds | c_1 | c_2 |
|----------|--------------|--------------------------|-------|
| GW170817 | c | 0.12357×10^{-4} | 6.967 |
| | $c/\sqrt{3}$ | 0.12179×10^{-4} | 6.967 |
| GW190425 | c | 0.870×10^{-6} | 7.605 |
| | $c/\sqrt{3}$ | 0.088×10^{-6} | 8.422 |

4.2. GW190814: A Postulation of the Most Massive Neutron Star

The GW190814 event that arised from the merger of a $\sim 23 M_{\odot}$ black hole with a $\sim 2.6 M_{\odot}$ compact object has provide various scenarios for the nature of the second component. In particular, the possibilities for the second merger component are that of (a) the lightest black hole, (b) the most compact neutron star, (c) a rapidly rotating neutron star (see Fig. 7), and (d) an exotic compact object. We note that in the present review, we considering only the scenarios where the compact object is a nonrotating neutron star or is a rapidly rotating one [66].

In Fig. 7 we display the gravitational mass as a function of the Kerr parameter for the pure MDI-APR EoS. In addition, we note the universal relation

$$M_{\text{rot}} = M_{\text{TOV}} \left[1 + 0.132 \left(\frac{\mathcal{K}}{\mathcal{K}_{\text{max}}} \right)^2 + 0.071 \left(\frac{\mathcal{K}}{\mathcal{K}_{\text{max}}} \right)^4 \right], \quad (63)$$

where \mathcal{K}_{max} is the Kerr parameter at the mass-shedding limit, for two limiting cases: (a) $M_{\text{TOV}} = 2.08 M_{\odot}$ and (b) $M_{\text{TOV}} = 2.3 M_{\odot}$ [140], and $\mathcal{K}_{\text{max}} = 0.68$. The limiting cases correspond to the minimum and maximum possible mass for a neutron star [140], along with the maximum value of the Kerr parameter (considering the minimum possible mass) [140]. The area marked by the intersection of the gravitational mass, $M = 2.59^{+0.08}_{-0.09} M_{\odot}$, with the Kerr parameter, $\mathcal{K} = [0.49, 0.68]$ [140], notes the area where the compact object can exist. Figures 1 and 7 show that the pure MDI-APR EoS, which is well-defined in the above limits, is a suitable hadronic EoS to describe the $\sim 2.6 M_{\odot}$ compact object.

Furthermore, by assuming that the second merger component is rotating at its mass-shedding limit, possible constraints are available through the Kerr parameter, the equatorial radius, and the central energy/baryon density. Specifically, by employing the relation found in Ref. [63]

$$\mathcal{K}_{\text{max}} = 0.488 + 0.074 \left(\frac{M_{\text{max}}}{M_{\odot}} \right), \quad (64)$$

for the observable gravitational mass, the maximum Kerr parameter is evaluated in the range $\mathcal{K}_{\text{max}} = [0.67, 0.69]$, a feature that is also noted in Fig. 7. Moreover, taking into consideration the relation from Ref. [64] that connects the Kerr parameter with the compactness parameter at the mass-shedding limit, as

$$\mathcal{K}_{\text{max}} = 1.34 \sqrt{\beta_{\text{max}}} \quad \text{and} \quad \beta_{\text{max}} = \frac{G}{c^2} \frac{M_{\text{max}}}{R_{\text{max}}}, \quad (65)$$

the equatorial radius is calculated in the range $R_{\text{max}} = [14.77, 14.87]$ km.

Finally, we focused on the central energy/baryon density, a property that is connected to the time evolution of pulsars and the appearance of a possible phase transition. The above dependence is presented in Fig. 8, as the dependence of the maximum gravitational mass on both the central energy density and the central baryon density. Specifically, Figure 8 contains a wide range of hadronic EoSs (23 EoSs) [63] both at the nonrotating and maximally rotating configurations, the analytical solution of Tolman VII, the Eq. (66) denoted as

$$\frac{M}{M_{\odot}} = 4.25 \sqrt{\frac{10^{15} \text{ gr cm}^{-3}}{\varepsilon_c / c^2}}. \quad (66)$$

according to Ref. [63], the calculation data from Cook *et al.* [141] and Salgado *et al.* [142], and the recent data for the nonrotating and maximally rotating configurations both in the cases of $(v_s/c)^2 = 1/3$ and $(v_s/c)^2 = 1$ with the corresponding transition densities.

In addition, via Eq. (66), which is used for the description of the upper bound for the density of cold baryonic matter [63], the central energy density can be constrained in the narrow range $\varepsilon_c / c^2 = [2.53, 2.89] 10^{15} \text{ gr cm}^{-3}$. The latter indicates that neutron stars with higher values of central energy density cannot exist. Furthermore, Fig. 8 provide us the tools to extract the corresponding region for the central baryon density, that is $n_c = [7.27, 8.09] n_s$. It is worth mentioning that the cases that took effect in this review meet the limit for the central energy/baryon density as they are included in the region described under Eq. (66).

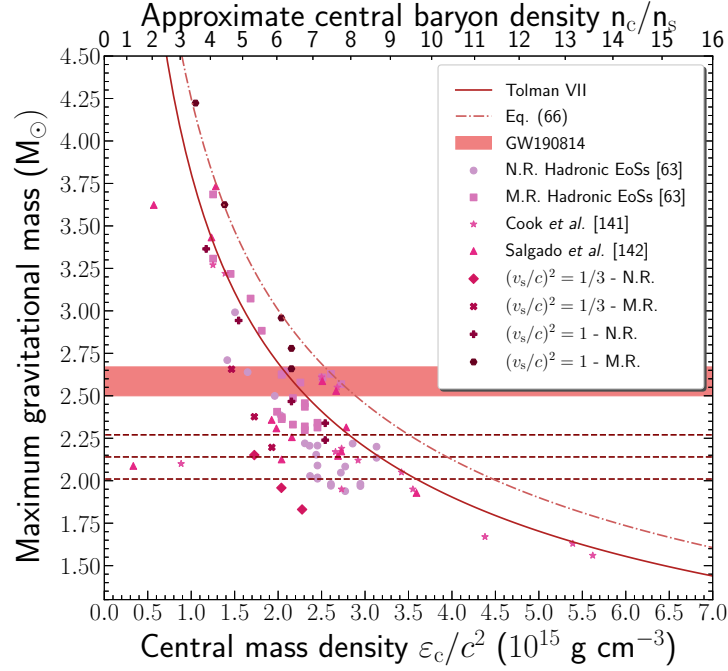


Figure 8. Dependence of the maximum gravitational mass on the central energy/baryon density both at nonrotating and rapidly rotating with the Kepler frequency configurations. Circles and squares correspond to 23 hadronic EoSs [63] at the non-rotating (N.R.) and maximally-rotating (M.R.) cases, respectively, and stars and triangles correspond to data of Cook *et al.* [141] and Salgado *et al.* [142], respectively. Furthermore, diamonds and pluses note the non-rotating configuration, while crosses and polygons note the maximally-rotating one, in the cases of the two limiting values of the sound speed. The horizontal dashed lines mark the current observed neutron star mass limits ($2.01 M_{\odot}$ [16], $2.14 M_{\odot}$ [17], and $2.27 M_{\odot}$ [18]). Eq. (66) is noted with the dashed-dotted line, while for comparison the Tolman VII analytical solution [63] is added with the solid line. The horizontal shaded region notes the mass range of the second component of GW190814 event.

4.3. The Case of a Very Massive Neutron Star

4.3.1. Isolated non-rotating neutron star

In this study we extended our previous work in Ref. [65] for an isolated non-rotating neutron star, by using two transition densities $n_{\text{tr}} = [1.5, 2]n_s$ and eight values of speed of sound bounds $(v_s/c)^2 = [1/3, 0.4, 0.5, 0.6, 0.7, 0.8, 0.9, 1]$ [66]. The values of transition density were taken to be close to the constraints of Ref. [65]. By solving numerically the system of TOV equations, combined with the previous bounds for the speed of sound, we obtained the M-R diagram, displayed in Fig. 9(a).

At first sight, there are two main branches in Fig. 9(a), related to the transition density. The solid (dashed) curves correspond to the $n_{\text{tr}} = 1.5n_s$ ($n_{\text{tr}} = 2n_s$) case. Depending on each value for the bound of the speed of sound, there are bifurcations in the families of EoSs. As we move to higher values for the speed of sound, the representing color of the curves is lightens. The blue solid horizontal line, with the accompanying shaded region, represents the estimation of the recently observed massive compact object of Ref. [19]. In general, the branch of EoSs with $n_{\text{tr}} = 1.5n_s$ provides stiffer EoSs compare to the $n_{\text{tr}} = 2n_s$ branch. Hence, the EoSs of the $n_{\text{tr}} = 1.5n_s$ case are more likely to provide such a massive non-rotating NS, than the $n_{\text{tr}} = 2n_s$ case in which three EoSs lie outside of the shaded region. Specifically, between

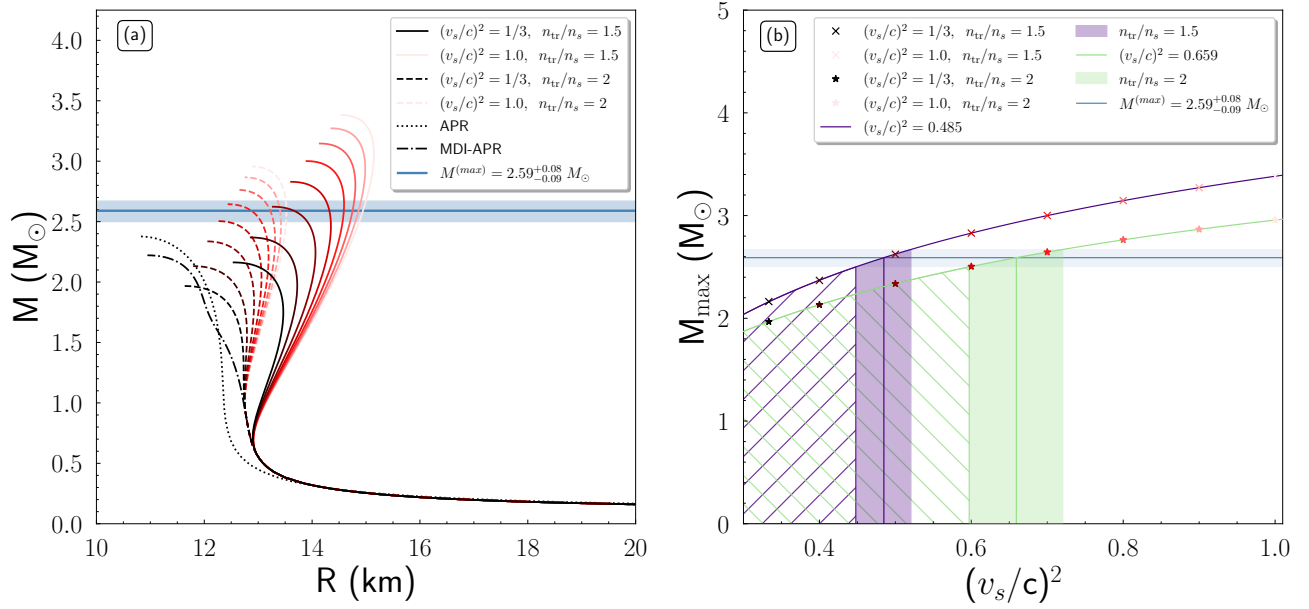


Figure 9. (a) Mass vs. radius for an isolated non-rotating NS, for each transition density n_{tr} and all speed of sound cases. The darker curves' color corresponds to the lower values of speed of sound. The blue horizontal line and region indicate the mass estimation of the massive compact object of Ref. [19]. The dashdot (dotted) curve corresponds to the MDI-APR (APR) EoS. (b) The maximum mass M_{max} of a non-rotating NS as a relation to the speed of sound bounds $(v_s/c)^2$ for each transition density n_{tr} (in units of saturation density n_s). The purple vertical shaded region corresponds to the $n_{tr} = 1.5n_s$ case, while the green one corresponds to the $n_{tr} = 2n_s$ case. The purple (green) vertical line indicates the corresponding value of the speed of sound for a massive object with $M = 2.59 M_\odot$.

the same kind of transition density n_{tr} the EoSs with higher speed of sound bounds lead to higher values of NS mass and radius. Therefore, a generally high bound of the speed of sound (as the transition density is getting higher values the speed of sound would be closer to the causal scenario) is needed for the description of such a massive compact object.

Table 3. Parameters of the Equation (67) and bounds of speed of sound value of Figure 9(b). The parameters c_1 , c_3 , and c_4 are in solar mass units M_\odot .

| n_{tr} | c_1 | c_2 | c_3 | c_4 | $(v_s/c)^2_{min}$ | $(v_s/c)^2$ | $(v_s/c)^2_{max}$ |
|----------|-----------------------|------------------------|------------------------|----------------------|-------------------|-------------|-------------------|
| $1.5n_s$ | -1.6033×10^3 | -7.56×10^{-4} | -1.64×10^{-1} | 1.6068×10^3 | 0.448 | 0.485 | 0.52 |
| $2n_s$ | 5.5754 | 0.2742 | -0.6912 | -1.9280 | 0.597 | 0.659 | 0.72 |

As one can observe in Fig. 9(a), there is a trend across the maximum masses. In order to study this behavior we constructed the diagram of Fig. 9(b). The cross (star) marks represent the maximum masses of $n_{tr} = 1.5n_s$ ($n_{tr} = 2n_s$) case. The color of the marks is getting lighter for higher values of the speed of sound. The blue solid horizontal line, with the accompanying shaded region, indicates the estimation of the recently observed massive compact object of Ref. [19]. The purple and green curves represent the following expression for the $n_{tr} = 1.5n_s$ and $n_{tr} = 2n_s$ case respectively, given below

$$M_{max} = c_1 d^{c_2} + c_3 d + c_4, \quad (67)$$

where $d = (v_s/c)^2$. The coefficients are given in Table 3.

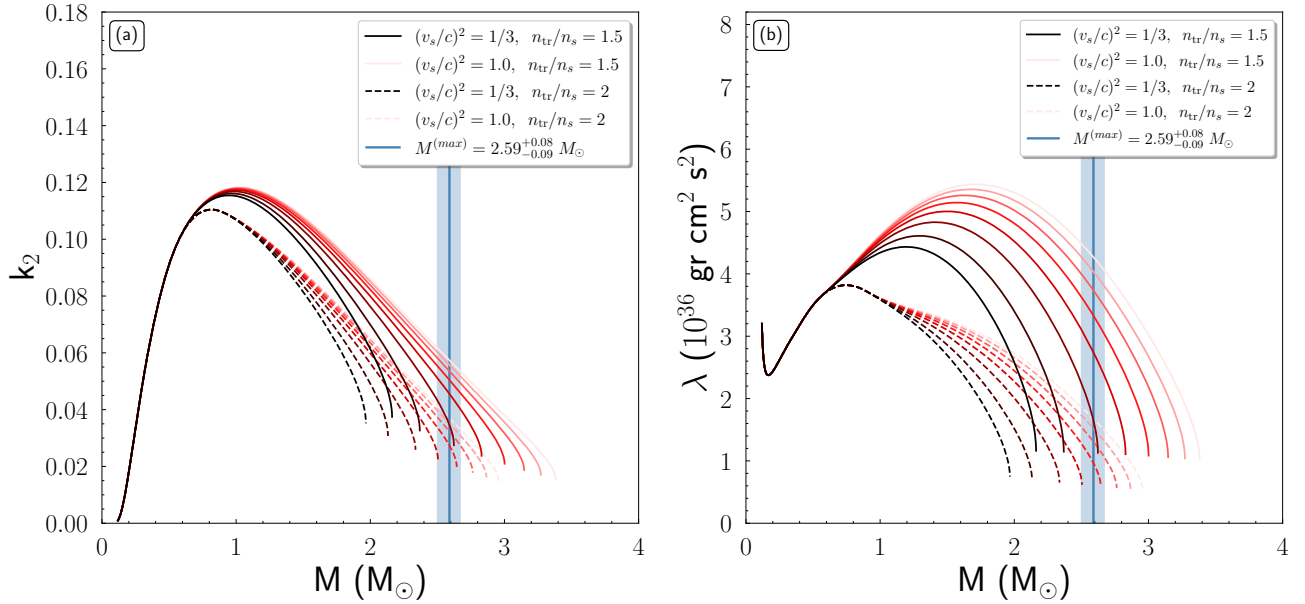


Figure 10. Tidal parameters (a) k_2 and (b) λ as a function of a NS's mass. The blue vertical line and shaded region indicate the estimation of the recently observed massive compact object of Ref. [19]. The solid (dashed) curves correspond to the $n_{\text{tr}} = 1.5n_s$ ($n_{\text{tr}} = 2n_s$) case. The lower values of the speed of sound correspond to the darker colored curves.

By applying the formula mentioned above, we were able to obtain estimations on the speed of sound values for each transition density n_{tr} . In particular, for a non-rotating massive NS with $M = 2.59 M_\odot$ the speed of sound must be (a) $(v_s/c)^2 = 0.485$ ($n_{\text{tr}} = 1.5n_s$), and (b) $(v_s/c)^2 = 0.659$ ($n_{\text{tr}} = 2n_s$). The exact values' interval is given in Table 3. We note that in the case of higher values of transition density n_{tr} the fitted expression and marks are shifted downwards, i.e. the higher the point of the transition in density, the smaller the provided maximum mass. In addition, as one can see in Fig. 9(b), the higher values of the speed of sound are more able to predict such massive NSs, until a specific boundary value of transition density n_{tr} (higher than those we adopted in our study) in which even the causality could not lead to such a massive NS.

Hence, a very massive non-rotating NS favors higher values of the speed of sound than the $v_s = c/\sqrt{3}$ limit. Based on our previous work, the current observation of NS mergers lead to a lower bound on the transition density n_{tr} [65]. At this point there is a contradiction that arises; the transition density n_{tr} must be above a specific lower value but not big enough so that can predict very massive masses.

In Fig. 10 we display the tidal parameters for the single NS case that we study as a function of the mass. The vertical blue shaded region and line indicate the mass estimation for the second compact object of Ref. [19]. One can observe that in both diagrams there are two main families of EoSs, distinguished by the transition density n_{tr} . The EoSs with higher speed of sound bounds lead to bigger values on both tidal parameters. This means that a NS with a higher speed of sound value is more deformable than a more compact one (with lower speed of sound value). Moreover, the EoSs with smaller transition density n_{tr} and higher $(v_s/c)^2$ values are more likely to predict a very massive NS of $M = 2.59 M_\odot$.

We notice that taking into consideration cases with higher transition density n_{tr} could lead to smaller values of tidal parameters, i.e. more compact stars and less deformable. Hence, a very high value of speed of sound, close to the causality, would be necessary to provide such a massive non-rotating NS.

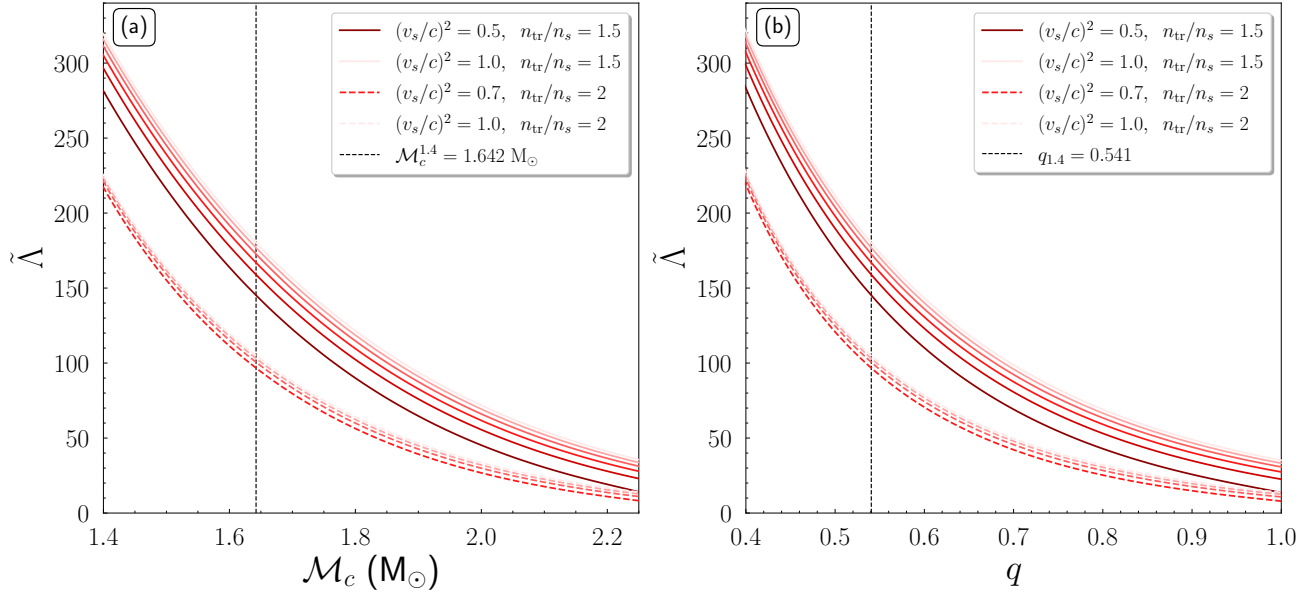


Figure 11. The effective tidal deformability $\tilde{\Lambda}$ as a function of (a) the chirp mass \mathcal{M}_c and (b) binary mass ratio q , in the case of a very massive NS component, identical to Ref. [19]. The darker colored curves correspond to lower values of speed of sound. The black dashed vertical line shows (a) the corresponding chirp mass \mathcal{M}_c and (b) mass ratio q , of a binary NS system with $m_1 = 2.59 M_\odot$ and $m_2 = 1.4 M_\odot$ respectively.

4.3.2. A very massive neutron star in a binary neutron stars system

Beyond the hypothetical scenario of a single non-rotating neutron star, it is of particular interest the binary case of two neutron stars, with the heavier to have a mass of $m_1 = 2.59 M_\odot$ and letting the secondary lighter neutron star to fluctuate within the range $m_2 \in (1, 2.59) M_\odot$. By subtracting the component masses m_1, m_2 in Eq. (18) we obtain the corresponding values of \mathcal{M}_c . Then, since the masses are defined, from the Eqs. (19) and (20), the effective tidal deformability $\tilde{\Lambda}$ can be determined.

In Fig. 11(a) we display the effective tidal deformability $\tilde{\Lambda}$ as a function of the chirp mass \mathcal{M}_c of the system, for all the possible binary NS systems with such a massive NS component. We have to underline that from all the EoSs that we studied in the single NS case previously, in the binary case we used only those who can provide a NS with $2.59 M_\odot$ mass. As one can see in Fig. 11, there are two families of EoSs, distinguished by the transition density n_{tr} . For each family of EoSs, the EoSs with higher value of the speed of sound predict higher values of $\tilde{\Lambda}$. We notice that for a binary system with $m_1 = 2.59 M_\odot$ and $m_2 = 1.4 M_\odot$ the chirp mass is $\mathcal{M}_c = 1.642 M_\odot$. Another remark is that binary NS systems with both heavy components, meaning higher \mathcal{M}_c , lead to smaller values of $\tilde{\Lambda}$. In this case, a possible lower limit on $\tilde{\Lambda}$ might provide useful constraints on the EoS.

In Fig. 11(b) we display the dependence of $\tilde{\Lambda}$ to the corresponding binary mass ratio q . We have to underline that this kind of $\tilde{\Lambda} - q$ diagram is different from the usual ones (see in comparison Fig. 3) because the chirp mass \mathcal{M}_c has not a specific value. Especially, in this work the \mathcal{M}_c is treated as a variable and each point of Fig. 11(b) corresponds to a different binary NS system with the heavier component in all cases to be a very massive NS with mass $2.59 M_\odot$. Similarly to Fig. 11(a) there are two main families for the curves and the EoSs with higher speed of sound provide higher values of $\tilde{\Lambda}$. The more symmetric binary NS systems ($q \rightarrow 1$) lead to smaller values of $\tilde{\Lambda}$. On the contrary, the highest values of $\tilde{\Lambda}$ correspond to the most asymmetric binary NS systems. We notice that for a binary system with $m_1 = 2.59 M_\odot$ and $m_2 = 1.4 M_\odot$ the asymmetry ratio is $q = 0.541$.

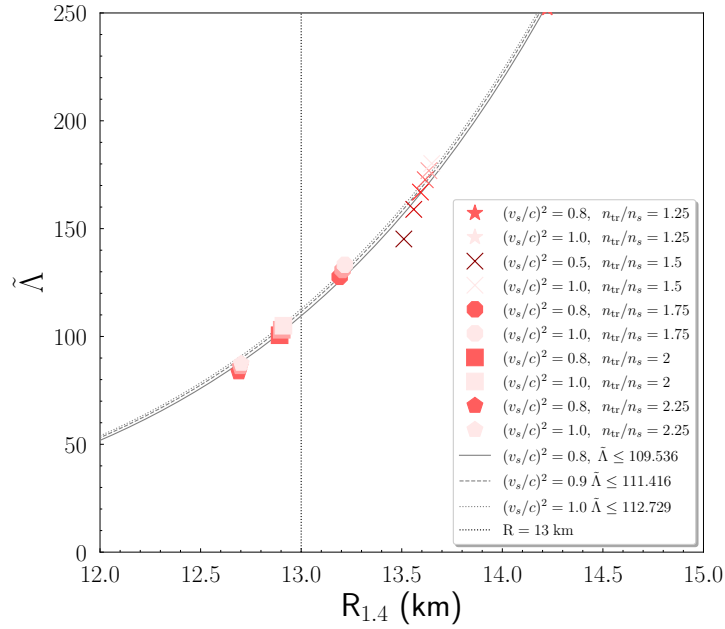


Figure 12. The effective tidal deformability $\tilde{\Lambda}$ as a function of the radius $R_{1.4}$ of a $m_2 = 1.4 M_\odot$ NS. The heavier component of the system was taken to be $m_1 = 2.59 M_\odot$. The darker colors correspond to lower values of speed of sound bounds. The grey lines show the expression of Equation (68). The black dotted vertical line indicates the proposed upper limit of Ref. [133].

Moreover, we studied the effective tidal deformability $\tilde{\Lambda}$ and the $R_{1.4}$ case of a $m_2 = 1.4 M_\odot$ secondary component NS, with the heavier component NS is taken to be $m_1 = 2.59 M_\odot$. In Fig. 12 we display this dependence. To be more specific, the EoSs are in five main groups, characterized by the transition density n_{tr} . Our study has been expanded to transition densities $n_{tr} = [1.25, 1.75, 2.25]$ so that the calculations could be more accurate. The higher speed of sound values correspond to lighter marks' color. In analog to the observations of the previous Fig. 11, the high speed of sound bounds lead to higher $\tilde{\Lambda}$ and $R_{1.4}$.

In addition, we applied a fitting formula to the $(v_s/c)^2 = [0.8, 0.9, 1]$ cases. The formula was taken to be in the kind of the proposed relations of Refs. [143,144].

$$\tilde{\Lambda} = c_5 R_{1.4}^{c_6}, \quad (68)$$

where the coefficients for each case are given in Table 4.

Table 4. Parameters of the Equation (68) and bounds of $\tilde{\Lambda}$ of Figure 12.

| $(v_s/c)^2$ | $c_5 \text{ (km}^{-1}\text{)}$ | c_6 | $\tilde{\Lambda}$ |
|-------------|--------------------------------|--------|-------------------|
| 0.8 | 4.1897×10^{-9} | 9.3518 | 109.536 |
| 0.9 | 5.3213×10^{-9} | 9.2652 | 111.416 |
| 1 | 6.1109×10^{-9} | 9.2159 | 112.729 |

According to a recent study, a similar power-law relation connects the tidal deformability of a single neutron star to the $R_{1.4}$ [145]. The significance of the tidal deformability $\Lambda_{1.4}$ and $R_{1.4}$ in order to obtain information about microscopic quantities was studied in Ref. [146]. Furthermore, Ref. [133] by imposing an upper limit on $R_{1.4}$ from Ref. [133], we obtained the constraints of Table 4.

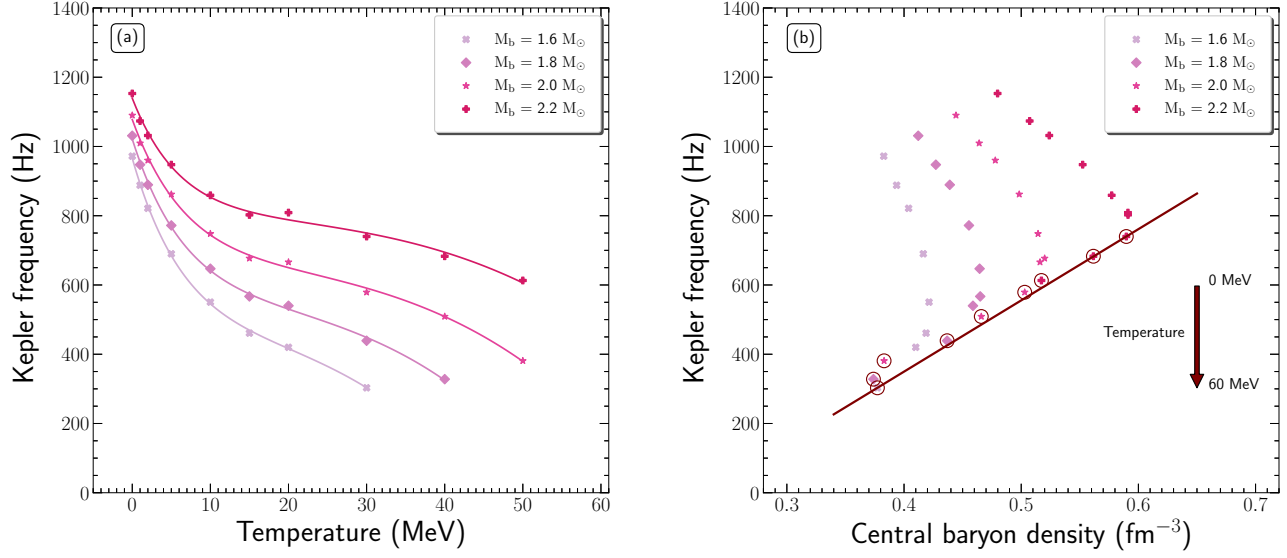


Figure 13. Dependence of the Kepler frequency on (a) the temperature and (b) the central baryon density for baryon masses in the range $[1.6, 2.2] M_{\odot}$. (a) Solid lines represent the fits originated from Eq. (69). (b) The solid line represents the Eq. (70), while open circles note the high-temperature region ($T \geq 30$ MeV).

4.4. Finite Temperature Effects on Rapidly Rotating Neutron Stars

4.4.1. Sequences of Constant Baryon Mass

A way to study the effects of finite temperature on the rapidly rotating remnant after a binary neutron star merger, is the sequences of constant baryon mass. The sequences provide us with information about the evolution and instabilities of hot neutron stars. In particular, in the case of the isothermal EoSs, we considered the same baryon mass configuration for the EoSs, and constructed a sequence related to the cooling of a hot neutron star [64].

In Fig. 13(a) is displayed the Kepler frequency as a function of the temperature for four baryon masses in the range $[1.6, 2.2] M_{\odot}$. Specifically, in the range $[0, 15]$ MeV the Kepler frequency decreases sharply with the temperature, while for higher temperatures a smoother behavior is presented. This dependence can be described as

$$f(T) = \alpha_0 + \alpha_1 T^3 + \alpha_2 \exp[\alpha_3 T] \quad (\text{Hz}), \quad (69)$$

where f and T are in units of Hz and MeV, respectively, and the coefficients α_i with $i = 0 - 3$ are given in Table 5.

Table 5. Coefficients α_i with $i = 0 - 3$ for the empirical relation (69) and baryon masses in the range $[1.6 - 2.2] M_{\odot}$.

| Coefficients | Baryon Mass | | | |
|------------------------|-----------------|-----------------|-----------------|-----------------|
| | $1.6 M_{\odot}$ | $1.8 M_{\odot}$ | $2.0 M_{\odot}$ | $2.2 M_{\odot}$ |
| $a_0 (\times 10^2)$ | 4.259 | 5.284 | 6.414 | 7.863 |
| $a_1 (\times 10^{-3})$ | -4.787 | -3.202 | -2.099 | -1.443 |
| $a_2 (\times 10^2)$ | 5.401 | 4.929 | 4.363 | 3.530 |
| $a_3 (\times 10^{-1})$ | -1.468 | -1.443 | -1.424 | -1.636 |

Afterwards, in Fig. 13(b) the dependence of Kepler frequency on the central baryon density is presented, for four baryon masses in the range $[1.6, 2.2] M_{\odot}$. While for low values

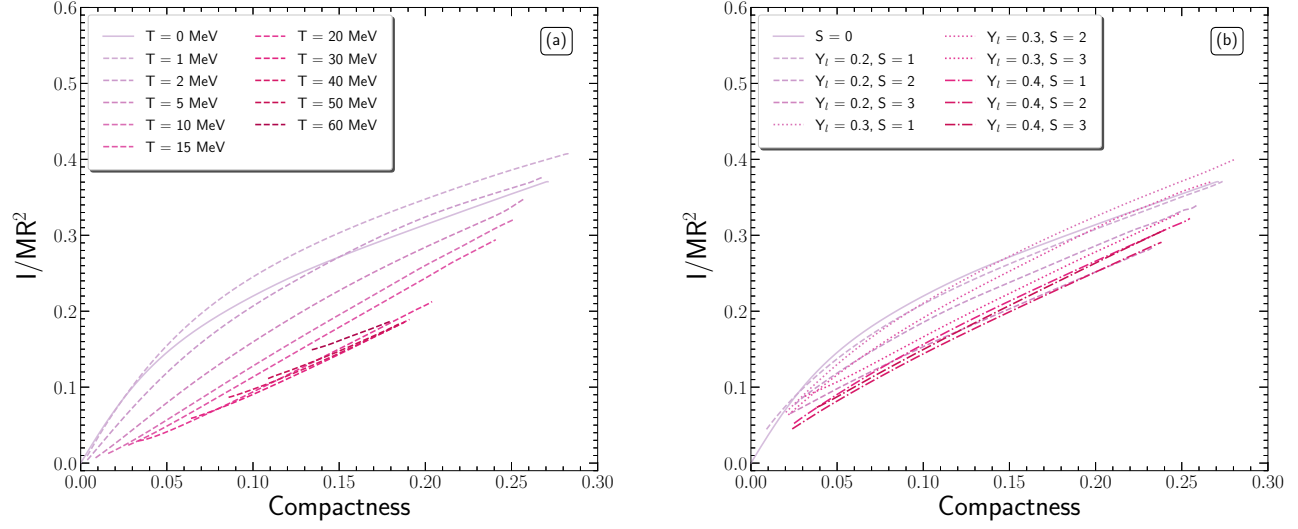


Figure 14. Dependence of the dimensionless moment of inertia on the compactness parameter at the mass-shedding limit in the case of (a) isothermal and (b) isentropic profiles. Dashed lines note the hot configurations, while solid line notes the cold one.

of temperature the central baryon density is increasing with increasing temperature, for high values of temperature, the a reduction on the values of the central baryon density is noted. The significance of the Fig. 13(b) is focused in temperatures higher than $T = 30$ MeV, where a linear relation described as

$$f(n_b^c) = -473.144 + 2057.271n_b^c \quad (\text{Hz}), \quad (70)$$

with f and n_b^c given in units of Hz and fm^{-3} , respectively, interpret the dependence of the Kepler frequency on the central baryon density independent from the specific baryon mass. Henceforth, Eq. (70) defines the allowed region that a neutron star can exist with rotation at its mass-shedding limit and for a specific central baryon density, and vice versa.

4.4.2. Moment of Inertia, Kerr parameter, and Ratio T/W

In Fig. 14 is displayed the dimensionless moment of inertia as a function of the compactness parameter for neutron stars at the mass-shedding limit in (a) isothermal profile and (b) in isentropic profile. In both cases, the increase of the temperature or the entropy per baryon (assuming a constant lepton fraction) leads to lower values of moment of inertia and lesser compact stars than the cold star. However, for low values of temperature ($T < 2$ MeV) or low values of entropy per baryon ($S = 1$ with $Y_l = 0.2$ and 0.3), the dimensionless moment of inertia and the compactness parameter exceed the values of the cold neutron star.

Afterwards, in Fig. 15 we present the Kerr parameter as a function of the gravitational mass for neutron stars at the mass-shedding limit (a) in isothermal profile and (b) in isentropic profile. In addition, we display the constraints for the Kerr parameter of neutron stars with the shaded region [64], and the Kerr bound for astrophysical Kerr black holes [98]. As the temperature or the entropy per baryon increases in the neutron star, the Kerr parameter decreases, except for high values of temperature ($T = 60$ MeV) where a slightly increase is observed. Furthermore, in Fig. 15(c) displayed in the isothermal profile the Kerr parameter as a function of the temperature for constant gravitational mass. After $T = 30$ MeV it is observed that the Kerr parameter creates a plate, meaning that the increase of temperature does not affect the Kerr parameter.

The introduction of temperature in neutron stars cannot violate the proposed limit for Kerr black holes [98] and the one from cold neutron stars [64]. Therefore, the gravitational collapse of a hot and uniformly rotating neutron star, constrained to mass-energy and angular momentum conservation, cannot lead to a maximally rotating Kerr black hole.

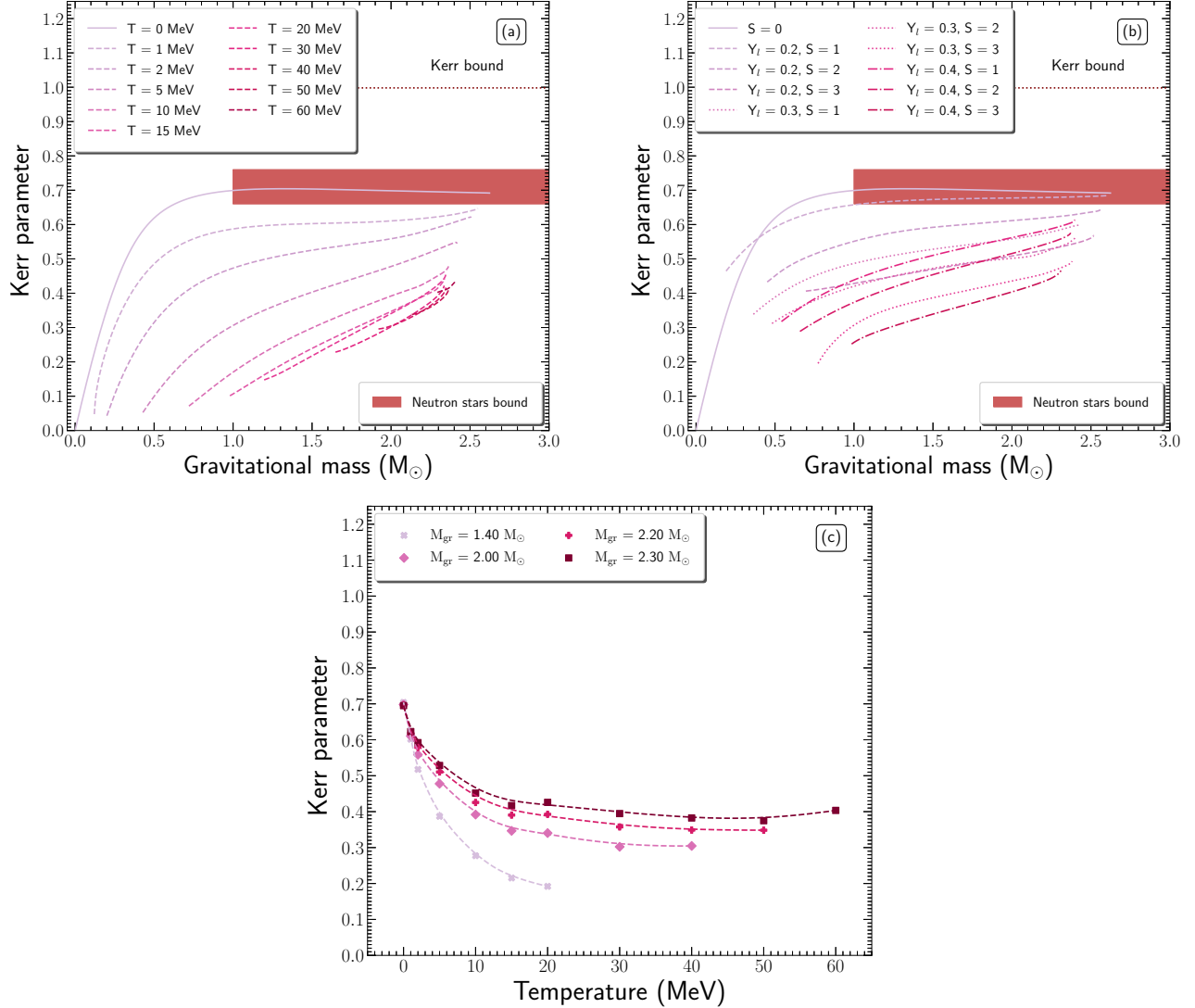


Figure 15. Dependence of the Kerr parameter on the gravitational mass at the mass-shedding limit in the case of (a) isothermal and (b) isentropic profiles. Dashed lines note the hot configurations, while solid line notes the cold one. The horizontal dotted line corresponds to the Kerr bound for astrophysical Kerr black holes, $\mathcal{K}_{B.H.} = 0.998$ [147], while the shaded region corresponds to the neutron star limits from Ref. [64]. (c) Dependence of the Kerr parameter on the temperature for gravitational masses in the range $[1.4, 2.2] M_\odot$ and in the case of isothermal profile.

In addition, it is worth mentioning that, while in the cold neutron star, for $M_{gr} > 1 M_\odot$, the Kerr parameter is almost independent of the gravitational mass, in hot configurations is an increasing function of the gravitational mass. The latter lead to the conclusion that while the interplay between the angular momentum and the gravitational mass in cold neutron stars is imperceptible, that's not the case in hot neutron stars, where a significant dependence is suggested.

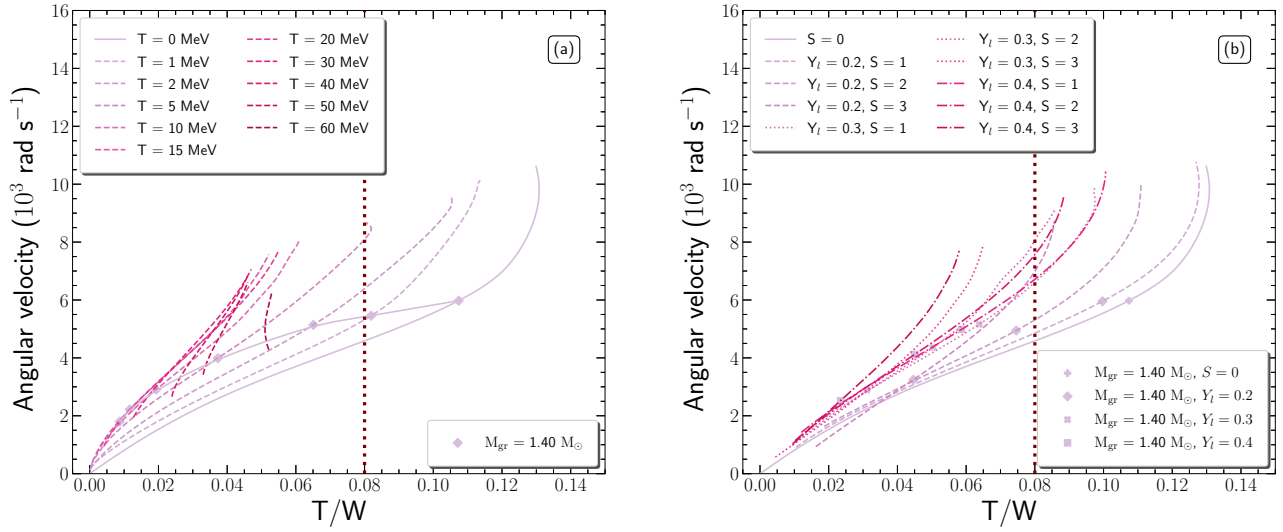


Figure 16. Dependence of the angular velocity on the ratio of rotational to kinetic gravitational binding energy at the mass-shedding limit in the case of (a) isothermal and (b) isentropic profiles. Dashed lines note the hot configurations, while solid line notes the cold one. Markers correspond to the $M_{\text{gr}} = 1.4 M_{\odot}$ configuration. The vertical dotted line notes the critical value, $T/W = 0.08$, for gravitational radiation instabilities.

Finally, in Fig. 16 is displayed the angular velocity as a function of the ratio of kinetic to gravitational binding energy T/W for neutron stars at the mass-shedding limit (a) in isothermal profile and (b) in isentropic profile. Gravitational waves can be produced from neutron stars through the nonaxisymmetric perturbations. The vertical dotted line notes the limit for nonaxisymmetric instabilities from gravitational radiation, located at $T/W \sim 0.08$ for models with $M_{\text{gr}} = 1.4 M_{\odot}$ [148]. The introduction of temperature leads to the conclusion that nonaxisymmetric instabilities cannot exist in hot neutron stars. However, for cases with low values of temperature ($T \leq 1 \text{ MeV}$ and $S = 1$ with $y_l = 0.2$), the nonaxisymmetric instability would set in before the mass-shedding limit is reached. The latter indicates that both the maximum gravitational mass and the angular velocity will be lowered.

The aftermath from the analysis on the compactness parameter, Kerr parameter, and ratio T/W , is the insight for the hot and rapidly rotating remnant after a neutron star merger. Actually, the remaining object is a compact object consisting of neutron star matter. By assuming a remnant with at least $T \geq 30 \text{ MeV}$ for isothermal neutron stars and $S = 1$ and $Y_l = 0.2$ for isentropic ones, rotating at its mass-shedding limit, possible constraints are available through the mentioned quantities. In particular,

- compactness parameter: $\beta_{\text{rem}}^{\text{iso}} \leq 0.19$ and $\beta_{\text{rem}}^{\text{ise}} \leq 0.27$,
- Kerr parameter: $\mathcal{K}_{\text{rem}}^{\text{iso}} \leq 0.42$ and $\mathcal{K}_{\text{rem}}^{\text{ise}} \leq 0.68$,
- ratio T/W : $(T/W)_{\text{rem}}^{\text{iso}} \leq 0.05$ and $(T/W)_{\text{rem}}^{\text{ise}} \leq 0.127$,

where the superscripts "iso" and "ise", correspond to isothermal and isentropic profiles [for more details see Ref. [64]]. To be more specific, in the case that the remnant follows the isothermal profile, the remaining object is a lesser compact object than the cold neutron star, with lower values of maximum gravitational mass and frequency, and stable toward the dynamical instabilities. In the case that the remnant follows the isentropic profile, the remaining object is comparable to the cold neutron star.

5. Concluding Remarks

In this review we have presented an EoS suitable parametrized to reproduce specific values of the speed of sound and gravitational mass of neutron stars. In addition, we introduced the effects of finite temperature both in isolated and in matters of merging neutron stars. In particular, we have constructed equilibrium sequences of both nonrotating and rapidly rotating with the Kepler frequency neutron stars and paid special attention to the gravitational and baryon mass, the radius, the transition baryon density, the Kerr parameter, the moment of inertia, the ratio T/W , and the tidal deformability. This study is applied in the several gravitational wave events, GW170817, GW190425, and GW190814, and possible constraints for the EoS are extracted.

Firstly, we studied the EoS, and especially imposed constraints on the speed of sound (which affects the stiffness of the EoS) and the transition density by using the recent observations of two binary neutron stars mergers (GW170817 and GW190425 events). The implemented method that we developed was based on the upper limits of the effective tidal deformability (derived from the mentioned events), combined with measurements of the maximum neutron star mass. As a base in our study we used the APR1-MDI EoS, for two cases of speed of sound bounds [75,149]; the conformal case $v_s = c/\sqrt{3}$ and the causal one of $v_s = c$.

The treatment of the effective tidal deformability as a function of the transition density allowed us to extract constraints on the speed of sound bounds. Specifically, for the GW170817 event we found that the speed of sound must be lower than the value $v_s = c/\sqrt{3}$ at least up to densities $n_{\text{tr}} \approx 1.6n_0$ and lower than $v_s = c$ up to densities $n_{\text{tr}} \approx 1.8n_0$. For the GW190425 event the respective values are $n_{\text{tr}} \approx n_0$ for the lower speed of sound bound and $n_{\text{tr}} \approx 1.2n_0$ for the upper one. These constraints are less rigorous than those derived from the GW170817 event.

Moreover, we studied the effective tidal deformability as a function of the maximum mass for both cases of speed of sound bounds. For the GW170817 we obtained that the maximum mass should be $M_{\text{max}} \leq 2.106 M_\odot$ for the $v_s = c/\sqrt{3}$ bound and $M_{\text{max}} \leq 3.104 M_\odot$ for the upper bound $v_s = c$. We notice that the limit of $M_{\text{max}} \approx 2.11 M_\odot$ corresponds to a transition density equal to $n_{\text{tr}} \approx 1.5n_0$. Hence, according to this finding, the conformal limit $v_s = c/\sqrt{3}$ is in contradiction with the observational estimations on the M_{max} of neutron stars. Therefore, it must be violated in order to be able to simultaneously describe small values of the effective tidal deformability and high values for neutron star mass. The reason for this contradiction is based on two different points of view that antagonize on another; the upper limit on $\tilde{\Lambda}$ favors softer EoSs (higher values of n_{tr}), while the maximum mass observational estimations require stiffer EoSs (smaller values of n_{tr}). For higher values of the speed of sound this contradiction becomes less present (e.g. $M_{\text{max}} \approx 3.1 M_\odot$ for the causal case $v_s = c$). We notice that the GW190425 was not able to offer further information.

Furthermore, from the study of the effective tidal deformability and the radius $R_{1.4}$ of a $1.4 M_\odot$ neutron star, we observed that all the EoSs follow a common trend. This trend is affected mainly by the chirp mass of the binary system. To be more specific, as the chirp mass gets higher values the trend moves downwards. From the event GW170817 we obtained an upper limit $R_{1.4} \approx 13$ km for both cases, which is consistent to other estimations. The event GW190425 provided an upper limit $R_{1.4} \approx 14.712$ km for the $v_s = c/\sqrt{3}$ bound and $R_{1.4} \approx 14.53$ km for the $v_s = c$ bound.

We postulate that the discovery of future events of binary neutron stars mergers will provide rich information and further constraints on the bound of the speed of sound. Especially, the detection of future events could lead to more stringent constraints on the upper limit of $\tilde{\Lambda}$, therefore more rigorous constraints on n_{tr} and the sound speed bounds. Based on our approach, the more useful events, for the lower limit of n_{tr} , would be those with lighter

component masses. Moreover, it would be of great interest to probe the lower limit of $\tilde{\Lambda}$. Such a lower limit might lead to an upper value on the transition density n_{tr} . We make the assumption that heavier neutron star mergers would be suitable in the direction of a possible upper limit on n_{tr} . In any case, further detection of neutron stars mergers will assist in these open problems.

The baryon mass of the postmerger remnant is considered approximately conserved, a feature that gives rise to the significance of the temperature. In particular, in the case of hot neutron stars, the baryon mass is lower than the cold ones. As remnants are considered rapidly rotating, we study them at the mass-shedding limit. Specifically, in the cold case, the baryon mass is $3.085 M_{\odot}$, while a hot one at $T = 30$ MeV is $2.427 M_{\odot}$ and one at $S = 1$ is $3.05 M_{\odot}$. By considering that the merger components have approximately equal masses, the above limits correspond to merger components with ~ 1.5425 , ~ 1.2135 , and $\sim 1.525 M_{\odot}$ baryon masses, respectively. Furthermore, the immediate aftermaths of GW170817 [13] and GW190425 [14] events had created hot and rapidly rotating remnants probably at the mass-shedding limit. In the case of GW170817 event, the remnant with $\sim 2.7 M_{\odot}$ can be supported under the uniform rotation of cold and isentropic neutron stars, with respect to the baryon mass of MDI+APR1 EoS. In contrast, isothermal neutron stars cannot support these values of mass. As far as concerning the GW190425 event, uniform rotation cannot interpret the remnant of $\sim 3.7 M_{\odot}$. It has to be noted that the postmerger remnant is assumed to rotate differentially. However, uniform rotation is a valid candidate to provide us with useful information about neutron stars.

In the GW190814 event [19], a compact object with a mass of $\sim 2.6 M_{\odot}$ had been observed, as a merger component. It is believed to be either the lightest black hole or the most massive neutron star [150]. Nonetheless, Most *et al.* [150] suggest that the compact object could be a neutron star rapidly spinning with \mathcal{K} in the range $[0.49, 0.68]$. In this case, the relevant postulation is in accordance with this study. More specific, the values of the gravitational mass and Kerr parameter coincide with the ones from the MDI+APR1 EOS in both cold catalyzed matter and isentropic matter with $S = 1$ and $Y_l = 0.2$. Following the latter conclusion, there is a possibility that the observed star was rotating close or at its mass-shedding limit and provide us additional constraints on the high density region of the nuclear EoS. In addition, possible constraints can be extracted for the corresponding equatorial radius. The Kerr parameter at the mass-shedding limit of the MDI+APR1 EoS lies in the region of $\mathcal{K}_{\text{max}} = [0.67, 0.69]$. This region also includes the upper limit of the relevant region from Ref. [150] in a narrow range. Furthermore, by exploiting the relation between the Kerr parameter and the compactness parameter, a possible tight region for the equatorial radius of the star is implied as $R_{\text{max}} = [14.77, 14.87]$ km.

The Kerr parameter has also the role of an indicator of the collapse to a black hole. In hot neutron stars, the Kerr parameter is relatively decreasing as the temperature inside the neutron star increases, and never exceeds the cold neutron star. In conclusion, thermal support cannot lead a rapidly rotating star to collapse into a maximally rotating Kerr black hole. In addition, after $\sim 1 M_{\odot}$, while the Kerr parameter is almost constant for the cold neutron stars, for hot neutron stars the Kerr parameter is increasing with respect to the gravitational mass. The latter, leads to a specific maximum value.

The ratio T/W is explicitly linked to the gravitational collapse to a black hole and the existence of stable supramassive neutron stars. We consider in the present study only the first case scenario. Instabilities originating from the gravitational radiation, in which the critical value is at $T/W \approx 0.08$ for the $M_{\text{gr}} = 1.4 M_{\odot}$ configuration [148], do not exist for hot neutron stars. Nonetheless, for low values of temperatures, as the ratio T/W exceeds the critical value, this limit sets the upper value for the maximum gravitational mass and angular velocity. It has to be noted that studies concerning the Kerr parameter, as well as the ratio

T/W , and the corresponding effect of the temperature are very rare. The existence of the latter studies may open a new window in neutron star studies.

A way to manifest the significance of the thermal support in neutron stars, is the evolutionary sequences of constant baryon mass. In this configuration, the dependence of the Kepler frequency on the central baryon density presents a linear relation for temperatures higher than $T = 30$ MeV. The existence of such a relation, independent from the baryon mass, can define the allowed region of the pair of the central baryon density and corresponding Kepler frequency for a rotating hot neutron star at its mass-shedding limit.

Central baryon/energy density can also be of great interest in cold neutron stars, as it is connected with the evolution of the neutron star and the possible appearance of a phase transition. The end point from our study, is that the central energy density must be lower than the values in the range $\varepsilon_c/c^2 = [2.53, 2.89] 10^{15} \text{ gr cm}^{-3}$, while for the central baryon density, the corresponding range is $n_c = [7.27, 8.09] n_s$. The latter can inform us about the stability of the neutron star, as a neutron star with higher values of central energy/baryon density cannot exist, as well as the appearance of the back-bending process.

Moreover, we examined the hypothetical scenario of a very massive neutron star with mass equal to $\sim 2.59_{-0.09}^{+0.08} M_\odot$, such as the secondary component of the GW190814 system [19]. In the case of a single non-rotating neutron star, the M-R diagram described in general the behavior of the EoSs. Furthermore, by studying the maximum mass of each EoS as a function of the speed of sound bounds (for each value of transition density n_{tr} , we were able to constrain the speed of sound. To be more specific, the $n_{\text{tr}} = 1.5n_s$ case leads to $(v_s/c)^2 \in [0.448, 0.52]$ while the $n_{\text{tr}} = 2n_s$ case leads to $(v_s/c)^2 \in [0.597, 0.72]$. We postulate that as the transition density n_{tr} is getting higher values, it is more difficult to achieve such a massive non-rotating NS. Especially, above a specific high transition density n_{tr} value, the speed of sound should be close to causality in order to provide such a massive NS.

By studying the tidal parameters for the single case, we observed that the lower transition densities n_{tr} lead to higher tidal parameters. Hence, the transition density $n_{\text{tr}} = 2n_s$ corresponds to a more compact NS (less deformation). Also, between the same kind of transition density n_{tr} , the EoSs with higher bounds on the speed of sound predict higher tidal parameters. Therefore, for the same transition density, the higher speed of sound bound means that the NS is less compact (more deformation).

Moving on the binary NS system case, we adopted the hypothesis of a very massive component with $m_1 = 2.59 M_\odot$, allowing us to investigate a variety of hypothetical binary NS systems with such a heavy component neutron star. In the case of both heavy component neutron stars, meaning high value for the system's chirp mass \mathcal{M}_c , the effective tidal deformability $\tilde{\Lambda}$ is getting smaller values (smaller deformation). This behavior was noticed also in the $\tilde{\Lambda} - q$ diagram, in which the increasing binary mass symmetric ratio q leads to smaller values of $\tilde{\Lambda}$. For a binary neutron system with the heavier component equal to $m_1 = 2.59 M_\odot$ and the lighter one equal to $m_2 = 1.4 M_\odot$, the chirp mass \mathcal{M}_c and the ratio q estimated to be $\mathcal{M}_c = 1.642 M_\odot$ and $q = 0.541$ respectively.

Lastly, we studied the case of a binary NS system with $m_1 = 2.59 M_\odot$ with a secondary component $m_2 = 1.4 M_\odot$. Especially, we concentrated on the radius $R_{1.4}$. A general remark is that the transition density $n_{\text{tr}} = 1.5n_s$ provides higher values of $R_{1.4}$ and $\tilde{\Lambda}$ than the $n_{\text{tr}} = 2n_s$ case. We extended our study to further transition densities n_{tr} , which confirmed this general behavior. Additionally, the higher speed of sound bounds provide higher values on both referred parameters. By imposing an upper limit on the radius, we extracted some upper limits on the $\tilde{\Lambda}$ for each value of speed of sound. Especially, this upper limit on $\tilde{\Lambda}$ shifts to higher values as the bound of the speed of sound is getting higher.

This hypothetical scenario of a very massive neutron star demonstrated the key role of a microscopic quantity of the EoS, the speed of sound, which affects dramatically the EoS in

combination with the changes in the transition density. We notice that the existence of such a massive non-rotating NS would mean a significant difference from all the so far known cases, consisting of a challenge in physics.

The underlying physics in neutron star mergers and the hot, rapidly rotating remnant should be investigated by considering differential rotation and cooling mechanisms, as these are the main features in the early postmerger phase. In addition, special emphasis should be given in the phase transition region, the existence of exotic degrees of freedom in the interior of neutron stars, as well as the accurate measurement of the tidal deformability. Finally, the observation of binary neutron star mergers and black hole - neutron star mergers, combined with the above studies, may provide significant constraints for the construction of the EoS.

Author Contributions: Conceptualization, P.S.K., A.K.P., and C.C.M.; Methodology, P.S.K. and A.K.P.; Software, P.S.K. and A.K.P.; Validation, P.S.K., A.K.P. and C.C.M.; Formal Analysis, P.S.K. and A.K.P.; Investigation, P.S.K., A.K.P., and C.C.M.; Data Curation, P.S.K. and A.K.P.; Writing - Original Draft Preparation, P.S.K., A.K.P., and C.C.M.; Writing - Review & Editing, P.S.K., A.K.P., and C.C.M.; Visualization, P.S.K., A.K.P., and C.C.M.; Supervision, C.C.M. All authors contributed equally to this work. All authors have read and agreed to the published version of the manuscript.

Funding: This research received no external funding.

Institutional Review Board Statement: Not applicable.

Informed Consent Statement: Not applicable.

Data Availability Statement: Not applicable.

Acknowledgments: The authors would like to thank Prof. K. Kokkotas for his constructive comments and insight during the preparation of the manuscript and also Prof. L. Rezzolla for useful corresponds and clarifications. The authors also thank Assistant Prof. B. Farr and Dr. Chatzioannou for providing computational tools regarding the kernel density estimation of the sample data and Profs. D. Radice, N. Stergioulas and N. Minkov for the useful correspondence. Acknowledgments also on Prof. P. Meszaros and Prof. A. Sedrakian for his useful comments regarding the hot equations of state. In addition, the authors wish to thank the Bulgarian Academy of Science and the organizers of the International Workshop "Shapes and Dynamics of Atomic Nuclei: Contemporary Aspects" (SDANCA-21) for the their hospitality while this was completed. We would like to thank the financial support of the Bulgarian National Science Fund under contracts No. KP-06-N48/1 and No. KP-06-N28/6.

Conflicts of Interest: The authors declare no conflict of interest.

Abbreviations

The following abbreviations are used in this manuscript:

| | |
|------|------------------------------------|
| EoS | Equation of state |
| MDI | Momentum dependent interaction |
| APR | Akmal, Pandharipande and Ravenhall |
| SNM | Symmetric Nuclear Matter |
| PNM | Pure Neutron Matter |
| N.R. | Non-rotating configuration |
| M.R. | Maximally-rotating configuration |

References

1. Shapiro, S.; Teukolsky, S. *Black Holes, White Dwarfs, and Neutron Stars*; John Wiley and Sons: New York, 1983.
2. Glendenning, N. *Compact Stars: Nuclear Physics, Particle Physics, and General Relativity*; Springer: Berlin, 2000.
3. Haensel, P.; Potekhin, A.; Yakovlev, D. *Neutron Stars 1: Equation of State and Structure*; Springer-Verlag: New York, 2007.
4. Weinberg, S. *Gravitational and Cosmology: Principle and Applications of the General Theory of Relativity*; Wiley: New York, 1972.
5. Zel'dovich, Y.B. The equation of state at ultrahigh densities and its relativistic limitations. *Sov. Phys. JETP* **1962**, *14*, 1143–1147.
6. Zel'dovich, Y.; Novikov, I. *Stars and Relativity*; Dover Publications, INC: Mineapolis New York, 1971.

7. Hartle, J.B. Bounds on the mass and moment of inertia of non-rotating neutron stars. *Phys. Rep.* **1978**, *46*, 201–247. doi:10.1016/0370-1573(78)90140-0.
8. Bedaque, P.; Steiner, A.W. Sound Velocity Bound and Neutron Stars. *Phys. Rev. Lett.* **2015**, *114*, 031103. doi:10.1103/PhysRevLett.114.031103.
9. Moustakidis, C.C.; Gaitanos, T.; Margaritis, C.; Lalazissis, G.A. Bounds on the speed of sound in dense matter, and neutron star structure. *Phys. Rev. C* **2017**, *95*, 045801. doi:10.1103/PhysRevC.95.045801.
10. Reed, B.; Horowitz, C.J. Large sound speed in dense matter and the deformability of neutron stars. *Phys. Rev. C* **2020**, *101*, 045803. doi:10.1103/PhysRevC.101.045803.
11. Van Oeveren, E.D.; Friedman, J.L. Upper limit set by causality on the tidal deformability of a neutron star. *Phys. Rev. D* **2017**, *95*, 083014. doi:10.1103/PhysRevD.95.083014.
12. Ma, Y.L.; Rho, M. Sound velocity and tidal deformability in compact stars. *Phys. Rev. D* **2019**, *100*, 114003. doi:10.1103/PhysRevD.100.114003.
13. Abbott, B.P.; others. GW170817: Observation of Gravitational Waves from a Binary Neutron Star Inspiral. *Phys. Rev. Lett.* **2017**, *119*, 161101. doi:10.1103/PhysRevLett.119.161101.
14. Abbott, B.P.; others. GW190425: Observation of a Compact Binary Coalescence with Total Mass $\sim 3.4 M_{\odot}$. *Astrophys. J.* **2020**, *892*, L3. doi:10.3847/2041-8213/ab75f5.
15. Arzoumanian, Z.; Brazier, A.; Burke-Spolaor, S.; Chamberlin, S.; Chatterjee, S.; Christy, B.; Cordes, J.M.; Cornish, N.J.; Crawford, F.; Cromartie, H.T.; Crowter, K.; DeCesar, M.E.; Demorest, P.B.; Dolch, T.; Ellis, J.A.; Ferdman, R.D.; Ferrara, E.C.; Fonseca, E.; Garver-Daniels, N.; Gentile, P.A.; Halmrast, D.; Huerta, E.A.; Jenet, F.A.; Jessup, C.; Jones, G.; Jones, M.L.; Kaplan, D.L.; Lam, M.T.; Lazio, T.J.W.; Levin, L.; Lommen, A.; Lorimer, D.R.; Luo, J.; Lynch, R.S.; Madison, D.; Matthews, A.M.; McLaughlin, M.A.; McWilliams, S.T.; Mingarelli, C.; Ng, C.; Nice, D.J.; Pennucci, T.T.; Ransom, S.M.; Ray, P.S.; Siemens, X.; Simon, J.; Spiewak, R.; Stairs, I.H.; Stinebring, D.R.; Stovall, K.; Swiggum, J.K.; Taylor, S.R.; Vallisneri, M.; van Haasteren, R.; Vigeland, S.J.; and, W.Z. The NANOGrav 11-year Data Set: High-precision Timing of 45 Millisecond Pulsars. *The Astrophysical Journal Supplement Series* **2018**, *235*, 37. doi:10.3847/1538-4365/aab5b0.
16. Antoniadis, J.; Freire, P.; Wex, N.; Tauris, T.; Lynch, R.; others. A massive pulsar in a compact relativistic binary. *Sci.* **2013**, *340*. doi:10.1126/science.1233232.
17. Cromartie, H.; Fonseca, E.; Ransom, S.; Demorest, P.B.; Arzoumanian, Z.; others. Relativistic Shapiro delay measurements of an extremely massive millisecond pulsar. *Nat. Astron.* **2019**. doi:10.1038/s41550-019-0880-2.
18. Linares, M.; Shahbaz, T.; Casares, J. Peering into the Dark Side: Magnesium Lines Establish a Massive Neutron Star in PSR J2215+5135. *Astrophys. J.* **2018**, *859*, 54. doi:10.3847/1538-4357/aabde6.
19. others, R.A. GW190814: Gravitational Waves from the Coalescence of a 23 Solar Mass Black Hole with a 2.6 Solar Mass Compact Object. *Astrophys. J.* **2020**, *896*, L44. doi:10.3847/2041-8213/ab960f.
20. Tan, H.; Noronha-Hostler, J.; Yunes, N. Neutron Star Equation of State in Light of GW190814. *Phys. Rev. Lett.* **2020**, *125*, 261104. doi:10.1103/PhysRevLett.125.261104.
21. Datta, S.; Phukon, K.S.; Bose, S. Recognizing black holes in gravitational-wave observations: Challenges in telling apart impostors in mass-gap binaries, 2021, [arXiv:gr-qc/2004.05974].
22. Alsing, J.; Silva, O.H.; Berti, E. Evidence for a maximum mass cut-off in the neutron star mass distribution and constraints on the equation of state. *Mon. Not. R. Astron. Soc.* **2018**, *478*, 1377. doi:10.1093/mnras/sty1065.
23. Farr, W.M.; Chatziioannou, K. A Population-Informed Mass Estimate for Pulsar J0740+6620. *Res. Not. Am. Astron. Soc.* **2020**, *4*, 65. doi:10.3847/2515-5172/ab9088.
24. Abbott, B.P.; Abbott, R.; Abbott, T.D.; others. GW170817: Measurements of Neutron Star Radii and Equation of State. *Phys. Rev. Lett.* **2018**, *121*, 161101. doi:10.1103/PhysRevLett.121.161101.
25. Bethe, H.; Brown, G.; Applegate, J.; Lattimer, J. Equation of state in the gravitational collapse of stars. *Nucl. Phys. A* **1979**, *324*, 487 – 533. doi:10.1016/0375-9474(79)90596-7.
26. Brown, G.; Bethe, H.; Baym, G. Supernova theory. *Nucl. Phys. A* **1982**, *375*, 481 – 532. doi:10.1016/0375-9474(82)90025-2.
27. Lamb, D.Q.; Lattimer, J.M.; Pethick, C.J.; Ravenhall, D.G. Hot Dense Matter and Stellar Collapse. *Phys. Rev. Lett.* **1978**, *41*, 1623–1626. doi:10.1103/PhysRevLett.41.1623.
28. Lattimer, J.M.; Ravenhall, D.G. Neutron star matter at high temperatures and densities. I. Bulk properties of nuclear matter. *Astrophys. J.* **1978**, *223*, 314–323. doi:10.1086/156265.
29. Lattimer, J.M. The Equation of State of Hot Dense Matter and Supernovae. *Ann. Rev. Nucl. Part. Sci.* **1981**, *31*, 337–374, [https://doi.org/10.1146/annurev.ns.31.120181.002005]. doi:10.1146/annurev.ns.31.120181.002005.
30. Lattimer, J.M.; Swesty, F.D. A generalized equation of state for hot, dense matter. *Nucl. Phys. A* **1991**, *535*, 331 – 376. doi:10.1016/0375-9474(91)90452-C.
31. Shen, H.; Toki, H.; Oyamatsu, K.; Sumiyoshi, K. Relativistic equation of state of nuclear matter for supernova and neutron star. *Nucl. Phys. A* **1998**, *637*, 435 – 450. doi:10.1016/S0375-9474(98)00236-X.
32. Shen, G.; Horowitz, C.J.; O'Connor, E. Second relativistic mean field and virial equation of state for astrophysical simulations. *Phys. Rev. C* **2011**, *83*, 065808. doi:10.1103/PhysRevC.83.065808.

33. Wellenhofer, C.; Holt, J.W.; Kaiser, N. Thermodynamics of isospin-asymmetric nuclear matter from chiral effective field theory. *Phys. Rev. C* **2015**, *92*, 015801. doi:10.1103/PhysRevC.92.015801.
34. Constantinou, C.; Muccioli, B.; Prakash, M.; Lattimer, J.M. Thermal properties of supernova matter: The bulk homogeneous phase. *Phys. Rev. C* **2014**, *89*, 065802. doi:10.1103/PhysRevC.89.065802.
35. Constantinou, C.; Muccioli, B.; Prakash, M.; Lattimer, J.M. Thermal properties of hot and dense matter with finite range interactions. *Phys. Rev. C* **2015**, *92*, 025801. doi:10.1103/PhysRevC.92.025801.
36. Sammarruca, F.; Machleidt, R.; Millerson, R. Temperature effects on the neutron matter equation of state obtained from chiral effective field theory. *Mod. Phys. Lett. A* **2020**, *35*, 2050156, [<https://doi.org/10.1142/S0217732320501564>]. doi:10.1142/S0217732320501564.
37. Nicotra, O. E.; Baldo, M.; Burgio, G. F.; Schulze, H.-J.. Protoneutron stars within the Brueckner-Bethe-Goldstone theory. *Astrophys. J.* **2006**, *451*, 213–222. doi:10.1051/0004-6361/20053670.
38. Burgio, G. F.; Schulze, H.-J.. The maximum and minimum mass of protoneutron stars in the Brueckner theory. *Astron. Astrophys.* **2010**, *518*, A17. doi:10.1051/0004-6361/201014308.
39. Baldo, M.; Burgio, G. The nuclear symmetry energy. *Prog. Part. Nucl. Phys.* **2016**, *91*, 203–258. doi:10.1016/j.ppnp.2016.06.006.
40. Fortin, M.; Taranto, G.; Burgio, G.F.; Haensel, P.; Schulze, H.J.; Zdunik, J.L. Thermal states of neutron stars with a consistent model of interior. *Mon. Not. R. Astron. Soc.* **2018**, *475*, 5010–5022, [<https://academic.oup.com/mnras/article-pdf/475/4/5010/24056722/sty147.pdf>]. doi:10.1093/mnras/sty147.
41. Lu, J.J.; Li, Z.H.; Burgio, G.F.; Figura, A.; Schulze, H.J. Hot neutron stars with microscopic equations of state. *Phys. Rev. C* **2019**, *100*, 054335. doi:10.1103/PhysRevC.100.054335.
42. Li, F.; Lu, J.J.; Li, Z.H.; Chen, C.Y.; Burgio, G.F.; Schulze, H.J. Accurate nuclear symmetry energy at finite temperature within a Brueckner-Hartree-Fock approach. *Phys. Rev. C* **2021**, *103*, 024307. doi:10.1103/PhysRevC.103.024307.
43. Figura, A.; Lu, J.J.; Burgio, G.F.; Li, Z.H.; Schulze, H.J. Hybrid equation of state approach in binary neutron-star merger simulations. *Phys. Rev. D* **2020**, *102*, 043006. doi:10.1103/PhysRevD.102.043006.
44. Shang, X.L.; Li, A.; Miao, Z.Q.; Burgio, G.F.; Schulze, H.J. Nucleon effective mass in hot dense matter. *Phys. Rev. C* **2020**, *101*, 065801. doi:10.1103/PhysRevC.101.065801.
45. Wei, J.B.; Burgio, G.F.; Schulze, H.J.; Zappalà, D. Cooling of hybrid neutron stars with microscopic equations of state. *Mon. Not. R. Astron. Soc.* **2020**, *498*, 344–354, [<https://academic.oup.com/mnras/article-pdf/498/1/344/33710758/staa1879.pdf>]. doi:10.1093/mnras/staa1879.
46. Raithel, C.A.; Özel, F.; Psaltis, D. Finite-temperature Extension for Cold Neutron Star Equations of State. *Astrophys. J.* **2019**, *875*, 12. doi:10.3847/1538-4357/ab08ea.
47. Pons, J.A.; Reddy, S.; Prakash, M.; Lattimer, J.M.; Miralles, J.A. Evolution of Proto-Neutron Stars. *Astrophys. J.* **1999**, *513*, 780–804. doi:10.1086/306889.
48. Prakash, M.; Lattimer, J.; Pons, J.; Steiner, A.; Reddy, S. Evolution of a Neutron Star From its Birth to Old Age. *Lect. Not. Phys.* **2001**, *578*, 364–423. doi:10.1007/3-540-44578-1.
49. Lattimer, J.M.; Prakash, M. The equation of state of hot, dense matter and neutron stars. *Phys. Rep.* **2016**, *621*, 127–164. Memorial Volume in Honor of Gerald E. Brown, doi:10.1016/j.physrep.2015.12.005.
50. Perego, A.; Bernouzzi, S.; Radie, D. Thermodynamics conditions of matter in neutron star mergers. *Europ. Phys. J. A* **2019**, *55*, 124. doi:10.1140/epja/i2019-12810-7.
51. Bauswein, A.; Janka, H.T.; Oechslin, R. Testing approximations of thermal effects in neutron star merger simulations. *Phys. Rev. D* **2010**, *82*, 084043. doi:10.1103/PhysRevD.82.084043.
52. Kaplan, J.D.; Ott, C.D.; O'Connor, E.P.; Kiuchi, K.; Roberts, L.; Duez, M. The Influence of Thermal Pressure on Equilibrium Models of Hypermassive Neutron Star Merger Remnants. *Astrophys. J.* **2014**, *790*, 19. doi:10.1088/0004-637x/790/1/19.
53. Tsokaros, A.; Ruiz, M.; Shapiro, S.L.; Sun, L.; Uryū, K.b.o. Great Impostors: Extremely Compact, Merging Binary Neutron Stars in the Mass Gap Posing as Binary Black Holes. *Phys. Rev. Lett.* **2020**, *124*, 071101. doi:10.1103/PhysRevLett.124.071101.
54. Yasin, H.; Schäfer, S.; Arcones, A.; Schwenk, A. Equation of State Effects in Core-Collapse Supernovae. *Phys. Rev. Lett.* **2020**, *124*, 092701. doi:10.1103/PhysRevLett.124.092701.
55. Radice, D.; Bernuzzi, S.; Perego, A. The Dynamics of Binary Neutron Star Mergers and GW170817. *Ann. Rev. Nucl. Part. Sci.* **2020**, *70*, null, [<https://doi.org/10.1146/annurev-nucl-013120-114541>]. doi:10.1146/annurev-nucl-013120-114541.
56. Sarin, N.; Lasky, P.D.; Ashton, G. Gravitational waves or deconfined quarks: What causes the premature collapse of neutron stars born in short gamma-ray bursts? *Phys. Rev. D* **2020**, *101*, 063021. doi:10.1103/PhysRevD.101.063021.
57. Soma, S.; Bandyopadhyay, D. Properties of Binary Components and Remnant in GW170817 Using Equations of State in Finite Temperature Field Theory Models. *Astrophys. J.* **2020**, *890*, 139. doi:10.3847/1538-4357/ab6a9e.
58. Sen, D. Nuclear matter at finite temperature and static properties of proto-neutron star. *J. Phys. G* **2020**, *48*, 025201. doi:10.1088/1361-6471/abcb9e.
59. Gale, C.; Bertsch, G.; Das Gupta, S. Heavy-ion collision theory with momentum-dependent interactions. *Phys. Rev. C* **1987**, *35*, 1666–1671. doi:10.1103/PhysRevC.35.1666.

60. Prakash, M.; Bombaci, I.; Prakash, M.; Ellis, P.J.; Lattimer, J.M.; Knorren, R. Composition and structure of protoneutron stars. *Phys. Rep.* **1997**, *280*, 1 – 77. doi:10.1016/S0370-1573(96)00023-3.
61. Li, B.A.; Schröder, W.U. *Isospin Physics in Heavy-Ion Collisions at Intermediate Energies*; New York: Nova Science, 2001.
62. Li, B.A.; Chen, L.W.; Ko, C.M. Recent progress and new challenges in isospin physics with heavy-ion reactions. *Phys. Rep.* **2008**, *464*, 113 – 281. doi:10.1016/j.physrep.2008.04.005.
63. Koliogiannis, P.S.; Moustakidis, C.C. Effects of the equation of state on the bulk properties of maximally rotating neutron stars. *Phys. Rev. C* **2020**, *101*, 015805. doi:10.1103/PhysRevC.101.015805.
64. Koliogiannis, P.S.; Moustakidis, C.C. Thermodynamical Description of Hot, Rapidly Rotating Neutron Stars, Protoneutron Stars, and Neutron Star Merger Remnants. *Astrophys. J.* **2021**, *912*, 69. doi:10.3847/1538-4357/abe542.
65. Kanakis-Pegios, A.; Koliogiannis, P.S.; Moustakidis, C.C. Speed of sound constraints from tidal deformability of neutron stars. *Phys. Rev. C* **2020**, *102*, 055801. doi:10.1103/PhysRevC.102.055801.
66. Kanakis-Pegios, A.; Koliogiannis, P.S.; Moustakidis, C.C. Probing the Nuclear Equation of State from the Existence of a $\sim 2.6 M_{\odot}$ Neutron Star: The GW190814 Puzzle. *Symmetry* **2021**, *13*, 183, [arXiv:astro-ph.HE/2012.09580]. doi:10.3390/sym13020183.
67. Sieniawska, M.; Bejger, M. Continuous Gravitational Waves from Neutron Stars: Current Status and Prospects. *Universe* **2019**, *5*, doi:10.3390/universe5110217.
68. Glampedakis, K.; Gualtieri, L., Gravitational Waves from Single Neutron Stars: An Advanced Detector Era Survey. In *The Physics and Astrophysics of Neutron Stars*; Rezzolla, L.; Pizzochero, P.; Jones, D.I.; Rea, N.; Vidaña, I., Eds.; Springer International Publishing: Cham, 2018; pp. 673–736. doi:10.1007/978-3-319-97616-7_12.
69. Andersson, N.; Kokkotas, K.D. The r-mode instability in rotating neutron stars. *International Journal of Modern Physics D* **2001**, *10*, 381–441, [https://doi.org/10.1142/S0218271801001062]. doi:10.1142/S0218271801001062.
70. Özel, F.; Freire, P. Masses, Radii, and the Equation of State of Neutron Stars. *Annual Review of Astronomy and Astrophysics* **2016**, *54*, 401–440, [https://doi.org/10.1146/annurev-astro-081915-023322]. doi:10.1146/annurev-astro-081915-023322.
71. Chatziioannou, K. Neutron-star tidal deformability and equation-of-state constraints. *Gen. Relativ. Gravit.* **2020**, *52*, 109. doi:10.1007/s10714-020-02754-3.
72. Prakash, M.; Bombaci, I.; Prakash, M.; Ellis, P.J.; Lattimer, J.M.; Knorren, R. Composition and structure of protoneutron stars. *Phys. Rep.* **1997**, *280*, 1 – 77. doi:10.1016/S0370-1573(96)00023-3.
73. Moustakidis, C.C. Effects of the nuclear equation of state on the *r*-mode instability and evolution of neutron stars. *Phys. Rev. C* **2015**, *91*, 035804. doi:10.1103/PhysRevC.91.035804.
74. Akmal, A.; Pandharipande, V.R.; Ravenhall, D.G. Equation of state of nucleon matter and neutron star structure. *Phys. Rev. C* **1998**, *58*, 1804–1828. doi:10.1103/PhysRevC.58.1804.
75. Margaritis, C.; Koliogiannis, P.S.; Moustakidis, C.C. Speed of sound constraints on maximally rotating neutron stars. *Phys. Rev. D* **2020**, *101*, 043023. doi:10.1103/PhysRevD.101.043023.
76. Rhoades, C.E.; Ruffini, R. Maximum Mass of a Neutron Star. *Phys. Rev. Lett.* **1974**, *32*, 324–327. doi:10.1103/PhysRevLett.32.324.
77. Kalogera, V.; Baym, G. The maximum mass of a neutron star. *Astrophys. J.* **1996**, *470*. doi:10.1086/310296.
78. Koranda, S.; Stergioulas, N.; Friedman, J.L. Upper Limits Set by Causality on the Rotation and Mass of Uniformly Rotating Relativistic Stars. *Astrophys. J.* **1997**, *488*, 799. doi:10.1086/304714.
79. Chamel, N.; Haensel, P.; Zdunik, J.; Fantina, A. On the Maximum Mass of Neutron Stars. *Int. J. Mod. Phys. E* **2013**, *22*, 1330018. doi:10.1142/S021830131330018X.
80. Podkowka, D.M.; Mendes, R.F.P.; Poisson, E. Trace of the energy-momentum tensor and macroscopic properties of neutron stars. *Phys. Rev. D* **2018**, *98*, 064057. doi:10.1103/PhysRevD.98.064057.
81. Xia, C.; Zhu, Z.; Zhou, X.; Li, A. Sound velocity in dense stellar matter with strangeness and compact stars. *Chin. Phys. C* **2021**, *45*, 055104. doi:10.1088/1674-1137/abea0d.
82. Tews, I.; Carlson, J.; Gandolfi, S.; Reddy, S. Constraining the Speed of Sound inside Neutron Stars with Chiral Effective Field Theory Interactions and Observations. *Astrophys. J.* **2018**, *860*, 149. doi:10.3847/1538-4357/aac267.
83. Feynman, R.; Metropolis, N.; Teller, E. Equations of State of Elements Based on the Generalized Fermi-Thomas Theory. *Phys. Rev.* **1949**, *75*, 1561. doi:10.1103/PhysRev.75.1561.
84. Baym, G.; Pethik, C.; Sutherland, P. The Ground State of Matter at High Densities: Equation of State and Stellar Models. *Astrophys. J.* **1971**, *170*, 299. doi:10.1086/151216.
85. Moustakidis, C.C. The stability of relativistic stars and the role of the adiabatic index. *Gen. Rel. Grav.* **2017**, *49*, 68. doi:10.1007/s10714-017-2232-9.
86. Lattimer, J.M.; Prakash, M. Neutron Star Structure and the Equation of State. *The Astrophys. J.* **2001**, *550*, 426–442. doi:10.1086/319702.
87. Postnikov, S.; Prakash, M.; Lattimer, J.M. Tidal Love numbers of neutron and self-bound quark stars. *Phys. Rev. D* **2010**, *82*, 024016. doi:10.1103/PhysRevD.82.024016.
88. Lattimer, J.M.; Prakash, M. Ultimate Energy Density of Observable Cold Baryonic Matter. *Phys. Rev. Lett.* **2005**, *94*, 111101. doi:10.1103/PhysRevLett.94.111101.

89. Lattimer, J.M.; Prakash, M. Nuclear matter and its role in supernovae, neutron stars and compact object binary mergers. *Physics Reports* **2000**, 333–334, 121–146. doi:[https://doi.org/10.1016/S0370-1573\(00\)00019-3](https://doi.org/10.1016/S0370-1573(00)00019-3).
90. Baiotti, L. Gravitational waves from neutron star mergers and their relation to the nuclear equation of state. *Prog. Part. Nucl. Phys.* **2019**, 109, 103714. doi:[10.1016/j.ppnp.2019.103714](https://doi.org/10.1016/j.ppnp.2019.103714).
91. Flanagan, E.E.; Hinderer, T. Constraining neutron-star tidal Love numbers with gravitational-wave detectors. *Phys. Rev. D* **2008**, 77, 021502. doi:[10.1103/PhysRevD.77.021502](https://doi.org/10.1103/PhysRevD.77.021502).
92. Hinderer, T. Tidal Love Numbers of Neutron Stars. *Astrophys. J.* **2008**, 677, 1216–1220. doi:[10.1086/533487](https://doi.org/10.1086/533487).
93. Damour, T.; Nagar, A. Relativistic tidal properties of neutron stars. *Phys. Rev. D* **2009**, 80, 084035. doi:[10.1103/PhysRevD.80.084035](https://doi.org/10.1103/PhysRevD.80.084035).
94. Hinderer, T.; Lackey, B.D.; Lang, R.N.; Read, J.S. Tidal deformability of neutron stars with realistic equations of state and their gravitational wave signatures in binary inspiral. *Phys. Rev. D* **2010**, 81, 123016. doi:[10.1103/PhysRevD.81.123016](https://doi.org/10.1103/PhysRevD.81.123016).
95. Fattoyev, F.J.; Carvajal, J.; Newton, W.G.; Li, B.A. Constraining the high-density behavior of the nuclear symmetry energy with the tidal polarizability of neutron stars. *Phys. Rev. C* **2013**, 87, 015806. doi:[10.1103/PhysRevC.87.015806](https://doi.org/10.1103/PhysRevC.87.015806).
96. Lackey, B.D.; Wade, L. Reconstructing the neutron-star equation of state with gravitational-wave detectors from a realistic population of inspiralling binary neutron stars. *Phys. Rev. D* **2015**, 91, 043002. doi:[10.1103/PhysRevD.91.043002](https://doi.org/10.1103/PhysRevD.91.043002).
97. Takátsy, J.; Kovács, P. Comment on “Tidal Love numbers of neutron and self-bound quark stars”. *Phys. Rev. D* **2020**, 102, 028501. doi:[10.1103/PhysRevD.102.028501](https://doi.org/10.1103/PhysRevD.102.028501).
98. Thorne, K.S. Tidal stabilization of rigidly rotating, fully relativistic neutron stars. *Phys. Rev. D* **1998**, 58, 124031. doi:[10.1103/PhysRevD.58.124031](https://doi.org/10.1103/PhysRevD.58.124031).
99. Abbott, B.P.; Abbott, R.; Abbott, T.D.; others. Properties of the Binary Neutron Star Merger GW170817. *Phys. Rev. X* **2019**, 9, 011001. doi:[10.1103/PhysRevX.9.011001](https://doi.org/10.1103/PhysRevX.9.011001).
100. Friedman, J.L.; Stergioulas, N. *Rotating Relativistic Stars*; Cambridge Monographs on Mathematical Physics, Cambridge University Press, 2013. doi:[10.1017/CBO9780511977596](https://doi.org/10.1017/CBO9780511977596).
101. Takami, K.; Rezzolla, L.; Yoshida, S. A quasi-radial stability criterion for rotating relativistic stars. *Mon. Not. R. Astron. Soc. Lett.* **2011**, 416, L1–L5, [<https://academic.oup.com/mnrasl/article-pdf/416/1/L1/6140636/416-1-L1.pdf>]. doi:[10.1111/j.1745-3933.2011.01085.x](https://doi.org/10.1111/j.1745-3933.2011.01085.x).
102. Weih, L.R.; Most, E.R.; Rezzolla, L. On the stability and maximum mass of differentially rotating relativistic stars. *Mon. Not. R. Astron. Soc. Lett.* **2017**, 473, L126–L130, [<https://academic.oup.com/mnrasl/article-pdf/473/1/L126/24841378/slx178.pdf>]. doi:[10.1093/mnrasl/slx178](https://doi.org/10.1093/mnrasl/slx178).
103. Stergioulas, N. <http://www.gravity.phys.uwm.edu/rns/>, 1996.
104. Stergioulas, N.; Friedman, J.L. Comparing Models of Rapidly Rotating Relativistic Stars Constructed by Two Numerical Methods. *Astrophys. J.* **1995**, 444, 306. doi:[10.1086/175605](https://doi.org/10.1086/175605).
105. Komatsu, H.; Eriguchi, Y.; Hachisu, I. Rapidly rotating general relativistic stars. I - Numerical method and its application to uniformly rotating polytropes. *Mon. Not. R. Astron. Soc.* **1989**, 237, 355. doi:[10.1093/mnras/237.2.355](https://doi.org/10.1093/mnras/237.2.355).
106. Cook, G.; Shapiro, S.; Teukolsky, S. Rapidly rotating polytropes in general relativity. *Astrophys. J.* **1994**, 422, 227. doi:[10.1086/173721](https://doi.org/10.1086/173721).
107. Goodstein, D.L. *States of Matter*; Dove, New York, 1985.
108. Fetter, A.L.; Walecka, J.D. *Quantum Theory of Many-Particle Systems*; Dover, Mineola, New York, 2003.
109. Prakash, M. *The Equation of State and Neutron Star*; unpublished, 1994.
110. Burgio, G.F.; Baldo, M.; Nicotra, O.E.; Schulze, H.J. A microscopic equation of state for protoneutron stars. *Astrophys. J. Suppl.* **2007**, 308, 387–394. doi:[10.1007/s10509-007-9360-8](https://doi.org/10.1007/s10509-007-9360-8).
111. Xu, J.; Chen, L.W.; Li, B.A.; Ma, H.R. Effects of isospin and momentum dependent interactions on liquid–gas phase transition in hot asymmetric nuclear matter. *Phys. Lett. B* **2007**, 650, 348 – 353. doi:[10.1016/j.physletb.2007.05.035](https://doi.org/10.1016/j.physletb.2007.05.035).
112. Moustakidis, C.C. Temperature and momentum dependence of single-particle properties in hot asymmetric nuclear matter. *Phys. Rev. C* **2008**, 78, 054323. doi:[10.1103/PhysRevC.78.054323](https://doi.org/10.1103/PhysRevC.78.054323).
113. Moustakidis, C.C.; Panos, C.P. Equation of state for β -stable hot nuclear matter. *Phys. Rev. C* **2009**, 79, 045806. doi:[10.1103/PhysRevC.79.045806](https://doi.org/10.1103/PhysRevC.79.045806).
114. Tan, N.H.; Loan, D.T.; Khoa, D.T.; Margueron, J. Mean-field study of hot β -stable protoneutron star matter: Impact of the symmetry energy and nucleon effective mass. *Phys. Rev. C* **2016**, 93, 035806. doi:[10.1103/PhysRevC.93.035806](https://doi.org/10.1103/PhysRevC.93.035806).
115. Takatsuka, T.; Nishizaki, S.; Hiura, J. Particular Properties of Dense Supernova Matter. *Prog. Theor. Phys.* **1994**, 92, 779–802, [<https://academic.oup.com/ptp/article-pdf/92/4/779/5358408/92-4-779.pdf>]. doi:[10.1143/ptp/92.4.779](https://doi.org/10.1143/ptp/92.4.779).
116. Takatsuka, T. Hot Neutron Stars at Birth and Related Problems*. *Prog. Theor. Phys.* **1996**, 95, 901–912, [<https://academic.oup.com/ptp/article-pdf/95/5/901/5280763/95-5-901.pdf>]. doi:[10.1143/PTP.95.901](https://doi.org/10.1143/PTP.95.901).
117. Friedman, J.L.; Ipser, J.R.; Sorkin, R.D. Turning Point Method for Axisymmetric Stability of Rotating Relativistic Stars. *Astrophys. J.* **1988**, 325, 722. doi:[10.1086/166043](https://doi.org/10.1086/166043).
118. Sorkin, R.D. A Stability Criterion for Many Parameter Equilibrium Families. *Astrophys. J.* **1982**, 257, 847. doi:[10.1086/160034](https://doi.org/10.1086/160034).
119. Goussard, J.O.; Haensel, P.; Zdunik, J.L. Rapid uniform rotation of protoneutron stars. *Astron. Astrophys.* **1997**, 321, 822–834. doi:<http://aa.springer.de/papers/7321003/2300822.pdf>.
120. Marques, M.; Oertel, M.; Hempel, M.; Novak, J. New temperature dependent hyperonic equation of state: Application to rotating neutron star models and $I-Q$ relations. *Phys. Rev. C* **2017**, 96, 045806. doi:[10.1103/PhysRevC.96.045806](https://doi.org/10.1103/PhysRevC.96.045806).

121. LORENE. LORENE: Langage Objet pour la Relativité Numérique, 1998.
122. Miller, M.C.; Lamb, F.K.; Dittmann, A.J.; Bogdanov, S.; Arzoumanian, Z.; Gendreau, K.C.; Guillot, S.; Harding, A.K.; Ho, W.C.G.; Lattimer, J.M.; Ludlam, R.M.; Mahmoodifar, S.; Morsink, S.M.; Ray, P.S.; Strohmayer, T.E.; Wood, K.S.; Enoto, T.; Foster, R.; Okajima, T.; Prigozhin, G.; Soong, Y. PSR J0030+0451 Mass and Radius from NICER Data and Implications for the Properties of Neutron Star Matter. *The Astrophysical Journal* **2019**, *887*, L24. doi:10.3847/2041-8213/ab50c5.
123. Greif, S.K.; Raaijmakers, G.; Hebeler, K.; Schwenk, A.; Watts, A.L. Equation of state sensitivities when inferring neutron star and dense matter properties. *Monthly Notices of the Royal Astronomical Society* **2019**, *485*, 5363–5376, [<https://academic.oup.com/mnras/article-pdf/485/4/5363/28262089/stz654.pdf>]. doi:10.1093/mnras/stz654.
124. Radice, D.; Perego, A.; Zappa, F.; Bernuzzi, S. GW170817: Joint Constraint on the Neutron Star Equation of State from Multimessenger Observations. *The Astrophysical Journal* **2018**, *852*, L29. doi:10.3847/2041-8213/aaa402.
125. Tews, I.; Margueron, J.; Reddy, S. Critical examination of constraints on the equation of state of dense matter obtained from GW170817. *Phys. Rev. C* **2018**, *98*, 045804. doi:10.1103/PhysRevC.98.045804.
126. Radice, D.; Dai, L. Multimessenger parameter estimation of GW170817. *The European Physical Journal A* **2019**, *55*, 50, [<https://doi.org/10.1140/epja/i2019-12716-4>]. doi:10.1140/epja/i2019-12716-4.
127. Kiuchi, K.; Kyutoku, K.; Shibata, M.; Taniguchi, K. Revisiting the Lower Bound on Tidal Deformability Derived by AT 2017gfo. *The Astrophysical Journal* **2019**, *876*, L31. doi:10.3847/2041-8213/ab1e45.
128. Coughlin, M.W.; Dietrich, T.; Doctor, Z.; Kasen, D.; Coughlin, S.; Jerkstrand, A.; Leloudas, G.; McBrien, O.; Metzger, B.D.; O’Shaughnessy, R.; Smartt, S.J. Constraints on the neutron star equation of state from AT2017gfo using radiative transfer simulations. *Monthly Notices of the Royal Astronomical Society* **2018**, *480*, 3871–3878, [<https://academic.oup.com/mnras/article-pdf/480/3/3871/33043575/sty2174.pdf>]. doi:10.1093/mnras/sty2174.
129. Coughlin, M.W.; Dietrich, T.; Margalit, B.; Metzger, B.D. Multimessenger Bayesian parameter inference of a binary neutron star merger. *Monthly Notices of the Royal Astronomical Society: Letters* **2019**, *489*, L91–L96, [<https://academic.oup.com/mnrasl/article-pdf/489/1/L91/30032497/slz133.pdf>]. doi:10.1093/mnrasl/slz133.
130. Most, E.R.; Weih, L.R.; Rezzolla, L.; Schaffner-Bielich, J. New Constraints on Radii and Tidal Deformabilities of Neutron Stars from GW170817. *Phys. Rev. Lett.* **2018**, *120*, 261103. doi:10.1103/PhysRevLett.120.261103.
131. Foley, R.J.; Coulter, D.A.; Kilpatrick, C.D.; Piro, A.L.; Ramirez-Ruiz, E.; Schwab, J. Updated parameter estimates for GW190425 using astrophysical arguments and implications for the electromagnetic counterpart. *Monthly Notices of the Royal Astronomical Society* **2020**, *494*, 190–198, [<https://academic.oup.com/mnras/article-pdf/494/1/190/32982848/staa725.pdf>]. doi:10.1093/mnras/staa725.
132. Rezzolla, L.; Most, E.R.; Weih, L.R. Using Gravitational-wave Observations and Quasi-universal Relations to Constrain the Maximum Mass of Neutron Stars. *The Astrophysical Journal* **2018**, *852*, L25. doi:10.3847/2041-8213/aaa401.
133. Raithel, C.A.; Özel, F.; Psaltis, D. Tidal Deformability from GW170817 as a Direct Probe of the Neutron Star Radius. *Astrophys. J.* **2018**, *857*, L23. doi:10.3847/2041-8213/aabcbf.
134. Zhao, T.; Lattimer, J.M. Tidal deformabilities and neutron star mergers. *Phys. Rev. D* **2018**, *98*, 063020. doi:10.1103/PhysRevD.98.063020.
135. De, S.; Finstad, D.; Lattimer, J.M.; Brown, D.A.; Berger, E.; Biwer, C.M. Tidal Deformabilities and Radii of Neutron Stars from the Observation of GW170817. *Phys. Rev. Lett.* **2018**, *121*, 091102. doi:10.1103/PhysRevLett.121.091102.
136. Annala, E.; Gorda, T.; Kurkela, A.; Vuorinen, A. Gravitational-Wave Constraints on the Neutron-Star-Matter Equation of State. *Phys. Rev. Lett.* **2018**, *120*, 172703. doi:10.1103/PhysRevLett.120.172703.
137. Fasano, M.; Abdelsalhin, T.; Maselli, A.; Ferrari, V. Constraining the Neutron Star Equation of State Using Multiband Independent Measurements of Radii and Tidal Deformabilities. *Phys. Rev. Lett.* **2019**, *123*, 141101. doi:10.1103/PhysRevLett.123.141101.
138. Fattoyev, F.J.; Piekarewicz, J.; Horowitz, C.J. Neutron Skins and Neutron Stars in the Multimessenger Era. *Phys. Rev. Lett.* **2018**, *120*, 172702. doi:10.1103/PhysRevLett.120.172702.
139. Landry, P.; Essick, R.; Chatziioannou, K. Nonparametric constraints on neutron star matter with existing and upcoming gravitational wave and pulsar observations. *Phys. Rev. D* **2020**, *101*, 123007. doi:10.1103/PhysRevD.101.123007.
140. Most, E.R.; Papenfort, L.J.; Weih, L.R.; Rezzolla, L. A lower bound on the maximum mass if the secondary in GW190814 was once a rapidly spinning neutron star. *Mon. Not. R. Astron. Soc. Lett.* **2020**, *499*, L82–L86. doi:10.1093/mnrasl/slaa168.
141. Cook, G.; Shapiro, S.; Teukolsky, S. Rapidly Rotating Neutron Stars in General Relativity: Realistic Equations of State. *Astrophys. J.* **1994**, *424*, 823. doi:10.1086/173934.
142. Salgado, M.; Bonazzola, S.; Gourgoulhon, E.; Haensel, P. High precision rotating neutron star models 1: Analysis of neutron star properties. *Astron. Astrophys.* **1994**, *291*, 155.
143. Zhao, T.; Lattimer, J.M. Tidal deformabilities and neutron star mergers. *Phys. Rev. D* **2018**, *98*, 063020. doi:10.1103/PhysRevD.98.063020.
144. De, S.; Finstad, D.; Lattimer, J.M.; Brown, D.A.; Berger, E.; Biwer, C.M. Tidal Deformabilities and Radii of Neutron Stars from the Observation of GW170817. *Phys. Rev. Lett.* **2018**, *121*, 091102. doi:10.1103/PhysRevLett.121.091102.
145. Tsang, C.; Tsang, M.; Danielewicz, P.; Fattoyev, F.; Lynch, W. Insights on Skyrme parameters from GW170817. *Phys. Lett. B* **2019**, *796*, 1–5. doi:10.1016/j.physletb.2019.05.055.

-
146. Weih, J.B.; Lu, J.J.; Burgio, G.F.; Li, Z.H.; Schulze, H.J. Are nuclear matter properties correlated to neutron star observables? *Eur. Phys. J. A* **2020**, *56*, 63. doi:10.1140/epja/s10050-020-00058-3.
 147. Thorne, K.S. Disk-Accretion onto a Black Hole. II. Evolution of the Hole. *Astrophys. J.* **1974**, *191*, 507–520. doi:10.1086/152991.
 148. Morsink, S.M.; Stergioulas, N.; Blattnig, S.R. Quasi-normal Modes of Rotating Relativistic Stars: Neutral Modes for Realistic Equations of State. *Astrophys. J.* **1999**, *510*, 854–861. doi:10.1086/306630.
 149. Koliogiannis, P.S.; Moustakidis, C.C. Effects of the equation of state on the bulk properties of maximally rotating neutron stars. *Phys. Rev. C* **2020**, *101*, 015805. doi:10.1103/PhysRevC.101.015805.
 150. Most, E.R.; Papenfort, L.J.; Weih, L.R.; Rezzolla, L. A lower bound on the maximum mass if the secondary in GW190814 was once a rapidly spinning neutron star. *Mon. Not. R. Astron. Soc. Lett.* **2020**, *499*, L82–L86, [<https://academic.oup.com/mnrasl/article-pdf/499/1/L82/33842178/slaa168.pdf>]. doi:10.1093/mnrasl/slaa168.